university of groningen / faculty of science and engineering

Fabrication and Characterization of a Magnetic Tunnel Junction

Author:
Alessandro VITALE
(s5146607)

Supervisor:
Prof. Tamalika BANERJEE
Second examiner :
Prof. Georgios PALASANTZAS

Bachelor's Thesis
To fulfill the requirements for the degree of
Bachelor of Science in Physics
at the University of Groningen

June 27, 2025

Contents

Abstract

A 2 nm thin amorphous aluminum oxide layer was used as a tunnel barrier in $Co/Al_2O_3/Ni_{80}Fe_{20}$ tunnel junctions, achieving a tunneling magnetoresistance of up to 3.36 % at 75 K. TMR was observed to appreciably decrease with both an increase in temperature and bias voltage, exhibiting trends observed in literature despite a lack of data points. Furthermore, comparison with literature helped identify all alternative conduction paths to direct tunneling which contributed to the poor TMR obtained, making it possible to evaluate and suggest improvements to the fabrication method used. Furthermore, a metal/insulator/metal tunnel junction was fabricated and its resistance was observed to significantly increase with a decrease in temperature, improving the accuracy of Simmons model fitting as it did so.

Acknowledgments

I would first of all like to thank Prof. Tamalika Banerjee for offering me such a captivating topic. It made these past 12 weeks seem to pass by in a flash, if it was up to me I would have spent 12 months on an even more in depth exploration. I would also like to thank her for her support and valuable input without which it would have been impossible to reach a satisfactory conclusion to this research. I cannot fail to mention my daily supervisor Hitesh Chhabra. He has been a fantastic partner for his intelligence, kind, calm and focused demeanor as well as his willingness to accept my input throughout the many challenges that we faced. If it had been anyone else I doubt we would have been able to make it this far. I would also like to thank the rest of professor Banerjee's group for the wonderful sense of community that helped me settle in right away. Within the group I would like to mention Ishitro Bhaduri who always seemed to know the exact answer to all of our questions, especially helping us figure out the practical facets of the fabrication process. In that same vein I must also thank Sytze Tirion for his technical help, form showing us how to change the crystal monitor in the Temescal to helping us wire bond our last sample. Lastly I would like to thank Hans de Vries who's help in refueling and up-keeping the Temescal electron beam evaporator was crucial for obtaining our working devices, as well as all the professors that in the last three years taught me all the information I needed to understand this topic in depth.

On a more personal note I would like to thank my parents Filippo Vitale and Tiziana Petrella for instilling in me the values by which I live, and always pushing me and supporting me academically without ever making it feel like it was my duty to excel. My only real goal in life is to be as good of a role model for my future kids as they were for me. I would also like to thank my girlfriend Isabella Jimenez Schwartz (Bella) for being by my side and literally keeping me company every day despite the physical distance between us, her support was invaluable to help me keep my sanity throughout these three years.

1 Introduction

Magnetic Tunnel Junctions are a spintronics device which, in its simplest form, is an insulating tunnel barrier interposed between two ferromagnetic electrodes as per Figure [6]. What at first glance appears to be a structurally modest device has fascinated countless researchers ever since Michel Jullière first attempted to explain its magnetization-orientation dependent characteristics in 1975 [1]. Based on the principle of spin polarized tunneling, itself arising from the inherent exchange splitting of the ferromagnetic electrodes' densities of states, MTJs -as they are colloquially referred to- display a low and a high resistance state. These states respectively correspond to the device's parallel and anti parallel relative magnetization configurations pictured in Figure [6]. The normalized difference between the two resistances, the maximization of which has been the subject of decades of research, was denominated TMR, tunneling magnetoresistance. Recent efforts into developing novel crystalline tunnel barriers and revolutionary new electrode materials such as half metals, allowed for great leaps in the magnitudes of TMR achievable in magnetic tunnel junctions. These values advanced from the 16 percent observed at room temperature by J.S. Moodera et.al [2] and T. Miyazaki et.al [3] in 1994 -a great milestone for the time- to the hundreds of percent reached by Stuart S. P. Parkin et.al in 2004 via the use of crystalline MgO tunnel barriers [4]; and have been steadily growing ever since [5].

Driving and being driven by these advancements are the astonishing applications of MTJs, which mainly revolve around distinguishing between the two resistance states. Hence, progress in TMR values has allowed MTJ applications to become commercially viable, rapidly growing their niche in their respective industries. Magnetic Random Access Memories, or MRAM for short, are a perfect example. Conventional DRAMs read the state of a memory cell, comprised by a transistor and a capacitor, by the charge stored on the latter, MRAMs accomplish the same task by reading the resistance state of the MTJ. This allows MRAMs to have several desirable advantages, combining the DRAM's high writing endurance with the highly coveted non volatile nature inherent to MTJs, considerably lowering idle power consumption. The chase for higher TMR values improves the distinguishability of the 1 and 0 states, increasing the reliability of the MRAM's reading process [5]. Consequently, the goal of this thesis is to survey the extent to which the equipment available to the faculty can support the fabrication of pinhole free metal/insulator/metal tunnel barriers to obtain high TMR amorphous $Co/Al_2O_3/Ni_{80}Fe_{20}$ magnetic tunnel junctions. Furthermore, a focus will be placed on studying their characteristics at varying temperature and applied potential bias as an opportunity to delve deep into the physical properties of this fascinating device. Hence it will act as a jumping off point to later research into better performing, more complex MTJ configurations.

1.1 Thesis Outline

The following Chapter [2] will give a more comprehensive overview of all the knowledge needed to grasp the results of the following research. An explanation of the governing principles and most recent understanding of tunneling in tunnel junctions is given, followed by an in depth look into magnetization, ferromagnets, and the balance of energies therein, finally culminating in an outline of Jullière's model of tunneling magnetoresistance. Numerous advanced tools were employed during the course of the fabrication and characterization of the M/I/M and MTJ samples grown for this thesis, as such a description of their inner workings is in order and can be found in Chapter [3]. The fabrication and characterization methods followed throughout the research process are delineated thereafter in Chapter [4]. Lastly the results obtained are to be presented and discussed in Chapter [5].

2 Essential Background Literature

The following explanation of magnetic tunnel junctions employs knowledge from numerous aspects of the physical and chemical sciences. Consequently, a solid understanding of particular subject matters such as magnetization, tunneling and the part they play in polarized tunneling current must be achieved to fully grasp the subsequent discussion of the obtained results. Although these explanations might seem trivial to those experienced in the subject matter, it is understood that not all readers will have a firm grasp of all the concepts here presented. As such the following explanations will delve deep into each topic, providing reminders to the knowledgeable and thorough explanations to those in need.

2.1 An in Depth Look at M/I/M Tunneling

2.1.1 Single Electron Tunneling

Electron tunneling itself is a purely quantum mechanical phenomenon whereby the wavefunction of an electron is only attenuated by a potential barrier rather than reduced to zero as expected classically, Figure [1]. The electron, having part of its wavefunction on the other side of the barrier, will have a finite probability of being found beyond said barrier. In a metal, insulator, metal junction the energy gap between the Fermi level of the metals and the first conduction band of the insulator serves as a single potential barrier of finite width and height. A simple single particle treatment of the finite potential tunneling problem, with starting energy E, can be found in any book with an introduction to quantum mechanics such as P. Atkins' and R. Friedman's "Molecular Quantum Mechanics" [6]. To summarize, the solutions to the time independent Schrödinger equation in areas 1 and 3 will be in the shape of plane waves traveling to and from the barrier:

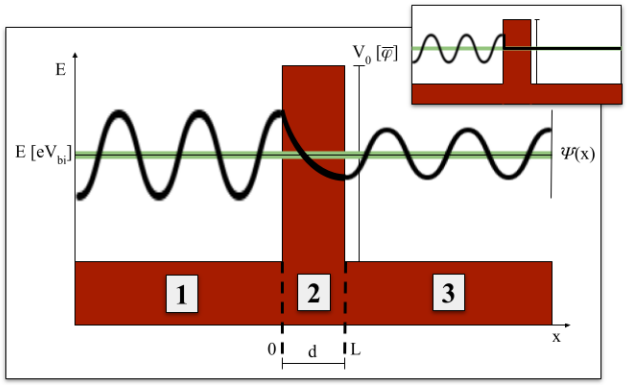

Figure 1: Potential landscape of the finite barrier tunneling problem with the wavefunction of the electron superimposed on it. Inset: the expected classical behavior of the wavefunction

$$\psi_1(x) = Ae^{ikx} + Be^{-ikx} \tag{1}$$

$$\psi_3(x) = Ee^{ikx} \tag{2}$$

where the term in $\psi_3(x)$ traveling back towards the barrier - Fe^{-ikx} - is ignored, due to area 1 being taken as the origin of the electron's motion. Whereas inside the tunnel barrier, area 2, the solutions will take the form of evanescent waves:

$$\psi_2(x) = Ce^{k'x} + De^{-k'x} \tag{3}$$

By attempting to satisfy the continuity condition of the wavefunction it is possible to obtain the following transmission coefficient as the ratio of transmitted to incident intensity:

$$T = \frac{|E|^2}{|A|^2} = \frac{1}{1 + (e^{\kappa L} - e^{-\kappa L})/[16(E/V_0)(1 - E/V_0)]} \tag{4}$$

for $\kappa = [2m^* V_0(1 - E/V_o)]^{1/2}/\hbar$ where m^* is the effective mass of the electron.

2.1.2 Tunneling in M/I/M Junctions

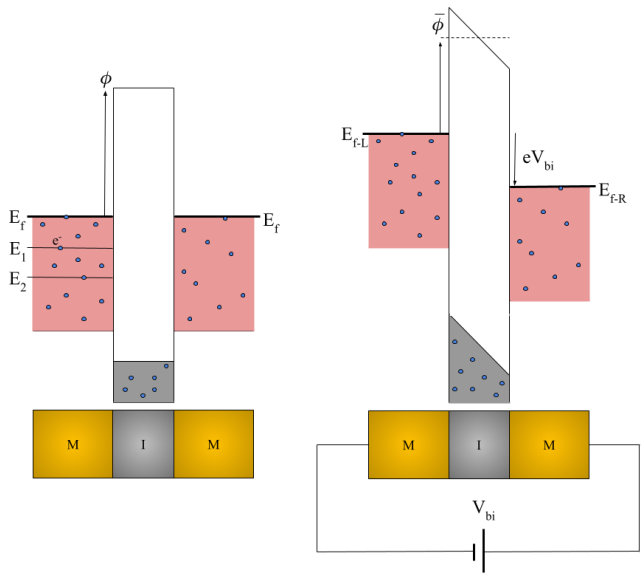

Figure 2: Potential landscape for the tunneling of electrons between two normal metal electrodes before and after the application of a potential bias, annotated with the quantities used by Simmons in his formulation of the problem

Applying this to an M/I/M junction however is not so trivial. In this scenario, multiple electrons will be able to tunnel from both electrodes, all of different energy dictated by the density of states (DOS) of the metals, the Fermi-Dirac distribution, as well as the applied potential difference, as illustrated in Figure [1]. The applied potential difference will also cause an offset in the Fermi energy levels, causing the tunnel barrier to become trapezoidal. Hence the transmission coefficient can no longer be solved exactly. R. Meservey and P. M. Tedrow's report on "Spin-Polarized Electron Tunneling" [7] helps shed light on how to model this problem with the aim of calculating the total tunneling current. In accordance to their formulation, the number of electrons tunneling from one electrode to the other per unit volume at energy E will be given by Fermi's Golden Rule. Namely it will be proportional to the density of states of the electrode at the energy level from which the electron derives, the density of states at the same energy in the recipient electrode and a matrix element $|M|^2$ containing all information on the tunneling probability of said electron. To adjust for the occupancy of the states at said energy in the origin electrode as well as vacancy of states at the same energy in the recipient electrode, this current density (I) will also be proportional to the Fermi-Dirac distribution as well as 1 - f at the same energy. Ensuring to adjust the densities of states and distributions for the bias on the junction this results in the following equations of current densities in both directions as well as total current [7]:

$$I_{l\to r}(V,E) \sim \rho_l(E)\rho_r(E+eV)|M|^2 f(E)[1-f(E+eV)] \tag{5}$$

$$I_{r\to l}(V,E) \sim \rho_l(E)\rho_r(E+eV)|M|^2 f(E+eV)[1-f(E)] \tag{6}$$

$$I_t(V) = \int_{-\infty}^{+\infty} \rho_l(E)\rho_r(E+eV)|M|^2[f(E)-f(E+eV)] \tag{7}$$

John G. Simmons [8] formulated a solution to this integral to be used as a practical model for tunneling experiments. To do so he employed the WKB approximation, a method to solve Schrodinger's equation when V slowly varies in x. By doing so he estimates the component of the wavefunction in the tunnel barrier - solved in detail in [9] - effectively replacing $\psi_2(x)$ in the previous calculation of the transmission coefficient. This results in the following general transmission coefficient for any shape tunnel barrier [8]:

$$T(E_x) \approx exp\{-\frac{4\pi}{h}\int_{s_1}^{s_2}[2m^*(V(x)-E_x)]^{\frac{1}{2}}dx\} \tag{8}$$

where s_1 and s_2 are the edges of the tunnel barrier at the Fermi level and E_x is the component of the particle's energy in the direction perpendicular to the M/I interface. Subsequently this T is taken as an

approximation of $|M|^2$ to calculate a general formula for tunnel current through any barrier shape. It is then adapted to a trapezoidal tunnel barrier taken as having average height $\bar{\phi}$ above the Fermi level (pre-applied bias). Further approximation by applying free particle densities of states and assuming 0 K, which transitions the equation for the Fermi-Dirac distribution:

$$f(E) = \frac{1}{e^{(E-E_F)/k_bT}+1} \tag{9}$$

to a step function, allowed Simmons to achieve the following result for current density (J):

$$J(V) \approx \frac{e}{2\pi h(\beta d)^2}\left\{(\bar{\phi}-\frac{eV}{2})\exp\left[-\frac{4\pi\beta d}{h}\sqrt{2m^*}\sqrt{\bar{\phi}-\frac{eV}{2}}\right]\right.$$
$$\left.-(\bar{\phi}+\frac{eV}{2})\exp\left[-\frac{4\pi\beta d}{h}\sqrt{2m^*}\sqrt{\bar{\phi}+\frac{eV}{2}}\right]\right\} \tag{10}$$

Where β is a correction factor for the integration of an arbitrary function which most of the time is ≈ 1 [8]. Important to later discussions is that this equation simplifies to a linear J(V) relationship at $V \approx 0$ and cubic for intermediate voltages $V < \varphi_0/e$ [8].

2.1.3 Further Corrections to the Description of M/I/M tunneling

As pointed out by Partick LeClair in his thesis on spin polarized tunneling [10] there are two glaring issues with this formulation. The first is the use of the average barrier height $\bar{\phi}$ which causes the J(V) characteristics to be symmetrical even for different electrodes, later corrected in multiple publications such as in the Brinkman model [11]. The second is that the resulting current density seems to be independent of the densities of states of the electrodes despite experiments on M/I/superconductor junctions by Giaever [12] showing a clear difference in the I(V) characteristics when switching from superconducting to normal metal states. This issue stems from Simmons and Brinkman simply adapting the single particle model explained before to multiple electrons, treating them as independent rather than interacting for the sake of obtaining a practical model. In doing so, as shown in later publications [13], these models obtained a matrix element with a direct dependence on the electron group velocity (dE/dk_x) due to it being present in the normalization of the plane wave wavefunctions in the two electrodes. This led to the canceling of the current's dependence on DOS in Equation [7] due to DOS being inversely proportional to electron group velocity ($[dE/dk_x]^{-1}$). While this model works well for normal metals, superconductors, or, of more relevance, ferromagnets are characterized by the many body interactions of electrons within them. A few years before Simmons two time Nobel laureate John Bardeen [14] used a many body approach which better described the framework of the problem to then obtain a refined single particle formulation. His approach consists of assigning the whole system a "ground state" wavefunction Ψ_0, describing it before the instance of tunneling, and an "excited state" wavefunction Ψ_{mn} describing it after the tunneling of an electron from state m on the left to state n on the right. He then defines a total time dependent wavefunction for the system as a linear combination of this ground state wavefunction and all possible excited states - representing the possible tunneling of any electron - and uses that to calculate the matrix element for transition m-n. This matrix element is only dependent on the Hamiltonian of the system and the identity of the initial and final wavefunctions, and thus is essentially a measure of the overlap of the initial and final states in the barrier Ψ_0 and Ψ_{mn}. Due to the lack of many body interactions in the barrier this simplifies to the overlap of single particle Ψ_m and Ψ_n states in the barrier which, as evidenced by Bardeen [14], thanks to the many body formulation, are not of the form of plane waves and thus independent of

electron velocity. This formulation of the matrix element thus avoids the unexpected neutralization of the DOS dependence in Equation [7]. Although this does not lead to a model that can be used to fit data in an experiment, the dependence of the current characteristics of tunnel junctions on the DOS of the electrodes is essential to understanding the reasoning behind the tunneling magnetoresistance observed in MTJs.

2.2 Origins and Consequences of Ordered Magnetization in Ferromagnets

2.2.1 Magnetization in Ferromagnets

In classical electrodynamics the total magnetic field B of a point in space is the sum of the magnetic field due to external, adjustable, sources - or free current - ($\mu_0 H$) and possible magnetization (μ_0M) generated by bound currents in materials present at that point [15]. In quantum mechanics however magnetization is defined as the sum of magnetic moments μ_i of the atoms in a material per unit volume, which themselves are the sum of spin and orbital angular momentum contributions [6]. Crucial for this treatment of MTJs is the distinction between linear materials, such as many paramagnets, in which M is related directly to H through a constant of proportionality named susceptibility χ [15] and non linear materials. The ferromagnets used as electrodes in MTJs are non linear; rather, a characterization of their M(H) will trace a hysteresis loop like the one shown in Figure [3] [15]. Unlike diamagnets, the elements that make up paramagnets and ferromagnets both have individual magnetic moments. The key distinction that changes their response to external magnetic fields is the strength of exchange interactions between the singular magnetic moments. One inescapable reality of our universe is that it inexorably tends towards energy minimization. The energy of the exchange interaction between two magnetic moments - directionally equivalent to spins -, given by the Heisenberg model formula shown below, is one such term that must be minimized [16]:

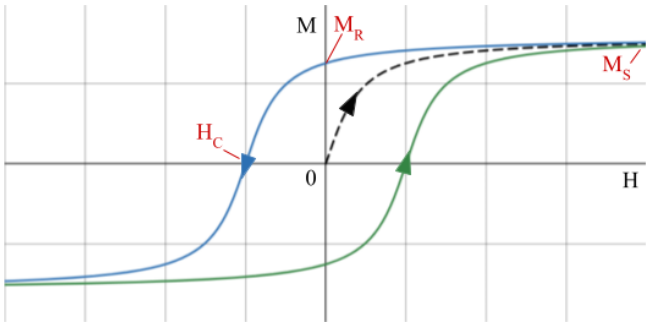

Figure 3: General hysteresis loop for a ferromagnet. Includes labels for coercive field H_C, saturation and remanent magnetizations M_S,M_R

$$U_{ex} = -2JS_i \cdot S_j = -2JS_iS_jcos\theta \tag{11}$$

To obtain the total exchange energy it is necessary to integrate over the contributions of all of atoms. J is the exchange integral, it is dependent on the overlap of the charge distributions of atoms i and j [16], and both its magnitude as well as sign have great repercussions on the classification of a material. A J low in magnitude results in a weak influence of the orientation of atoms on each other, easily overcome by thermal disorder, giving rise to paramagnetism. On the other hand, a sizable J will give the minimization of exchange energy a greater influence on the orientation of the individual magnetic moments in a material leading to ordered magnetism. Shifting to sign considerations, when J_{ex} is negative energy is minimized through an anti parallel orientation of the two atoms' spins (moments), giving rise to ferrimagnetism and antiferromagnetism. Of more interest for discussions on MTJs is when J_{ex} is positive, leading the system to prefer aligned spins, forming ferromagnets. However, there are many other contributions to the total magnetic energy of a ferromagnet that disturb this alignment. Of great influence is the minimization of magnetic energy. As perhaps more intuitively understood from the classical description of the atomic magnetic moment as a current loop generated by the

unpaired electron orbiting the nucleus, atomic magnetic moments are magnetic dipoles [15]. When magnetized in a singular direction, the poles of the individual moments align, and those nearest the surface won't be canceled, making the material a macroscopic magnetic dipole with a corresponding magnetic field as shown in Figure [4a]. This will result in high magnetic energy [16]:

$$U_{mag} = \frac{1}{8\pi} \int BdV \tag{12}$$

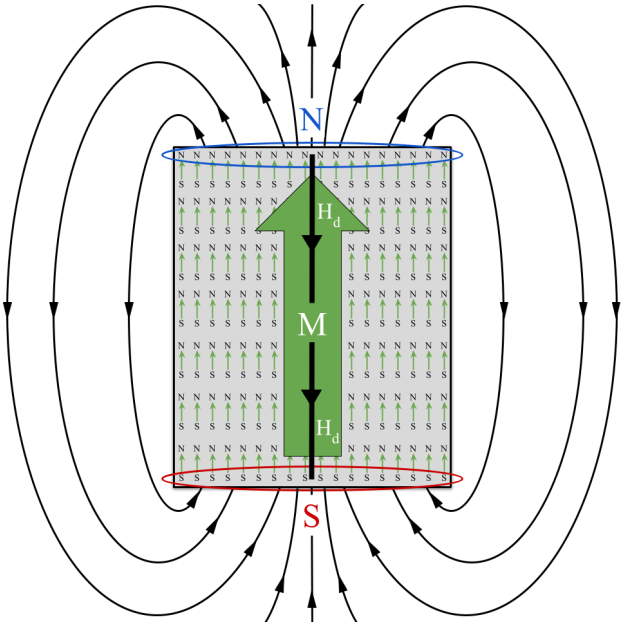

(a) Diagram of a 1 domain ferromagnet including demagnetizing field

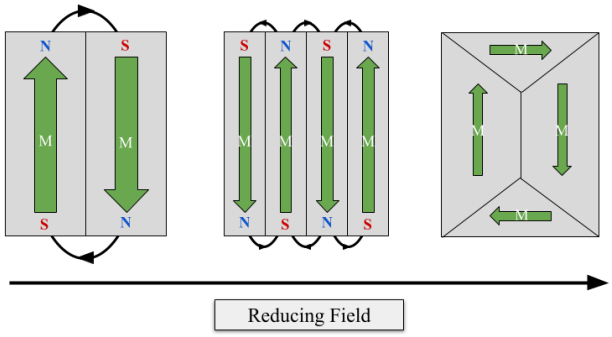

(b) Domain configuration that increasingly reduce magnetic energy, rightmost displays domains of closure

Figure 4: Figure displaying the reduction of energy by domains as well as the origin of shape anisotropy

To minimize the magnetic energy density domains are formed of opposite magnetization, with the most efficient configuration being domains of closure, shown in Figure [4b]. Domain formation however costs exchange energy at the domain walls, partially reduced by a gradual rotation of magnetizations rather than abrupt switches [16]. The creation of these macroscopic poles also results in a demagnetizing field H_d forming inside the material following the conventional north to south orientation, thus opposing magnetization. Consequently, magnetization will be more favorable along a long axis than a short one [17]. Anisotropy in magnetization direction can also come as a result of the structure in which the material crystallizes. Certain crystallographic directions are observed to be more favorable for magnetization such as the out of plane direction in hcp (hexagonal close packed) crystals. A more in depth explanation of this phenomenon is out of place in a discussion of MTJs, however can be found in Charles Kittel's "Introduction to Solid State Physics" [16]. In addition thermal energy leads to disorder in the directions of magnetic moments and can cause ferromagnets to transition to a paramagnetic phase beyond a critical Curie temperature T_c [16]. The last of the energy minimization considerations is what directly links the outside field H with the direction of magnetization. The energy of a magnetic moment in a magnetic field, having the following form [15]:

$$U_{field} = -\mu_i \cdot B \tag{13}$$

will be minimized when the individual magnetic moments align with the external magnetic field, giving them a preferential direction and thus growing magnetization M in the direction of the field. It is now possible to understand the shape of the hysteresis loop. Even ferromagnets will start with zero magnetization due to the nature of the domains described prior. As the external field is increased the volume of domains already oriented with the field will increase until they all point in the direction of the field, reaching a maximum "saturation magnetization". When the field is reduced once again to zero not all domains will switch back to their original directions due to defects in the material, resulting in a "remanent magnetization". Thus a "coercive field" in the opposite direction is needed to bring the ferromagnet back to zero magnetization and the cycle repeats [15][16].

2.2.2 Exchange Splitting

Strangely, many ferromagnetic materials appear to have non integral average Bohr magneton contributions per atom as evident in Table 1 of chapter 12 of Kittel's "Introduction to Solid State Physics" [16]. One reason for this anomaly, as Kittel mentions, is if there is an imbalance in the number of occupied spin up and spin down states, hinting at a spontaneous spin splitting of the density of states of the material. This exact reasoning is what led Edmund C. Stoner [19] to lay the foundations for the criterion used in the identification of ferromagnets, later given his name. As masterfully summarized by Dipanjan Mazumdar [20], the Stoner criterion is once again a matter of energy minimization. Under no influence of a magnetic field, suppose δn spin down electrons in the range $E_f - \delta E \rightarrow E_f$ have their spin flipped and will now be spin up electrons in the range $E_f \rightarrow E_f + \delta E$. The energy cost for this transition will be the number of electrons involved (n) times the energy difference (δE):

$$\Delta E_{cost} = n \cdot \delta E = \frac{1}{2}\rho(E_f)\delta E \cdot \delta E \qquad (14)$$

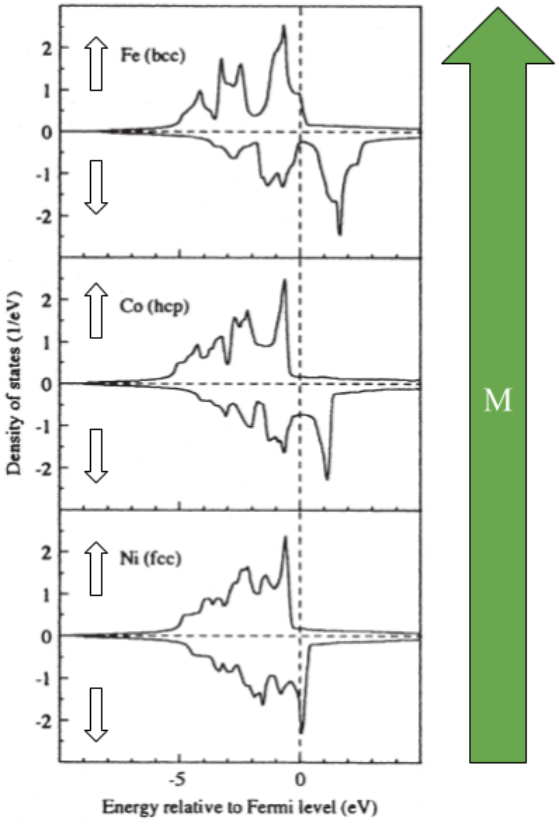

Figure 5: Exchange splitting of the densities of states of 3 ferromagnets Ni,Co and Fe. The graphs themselves originate from Doudin and Ansermet's work [18], adapted to show how the DOS of up and down spins split relative to an arbitrary magnetization direction

opposing this energy cost is the energy gained through the previously detailed exchange interactions, which, when generalized to the influence all electrons have on each other, can be seen as an average "exchange field" λM acting on each spin. Assuming a magnetic moment per electron of 1 μ_B the total magnetization will be $M = \mu_B(n_\uparrow - n_\downarrow)$ where $n_{\uparrow/\downarrow}$ are the number densities of up and down spins: $n_{\uparrow/\downarrow} = \frac{1}{2}(n \pm \rho(E_f)\delta E)$.

The energy gained from this field will then be:

$$\Delta E_{gain} = -\int_0^M \mu_0(\lambda M')dM = -\frac{1}{2}\mu_0\mu_B^2\lambda(n_\uparrow - n_\downarrow)^2 = -\frac{1}{2}U(\rho(E_f)\delta E)^2 \tag{15}$$

for U = $\mu_0\mu_B^2\lambda$. Consequently, the Stoner criterion states that when the energy gained from the exchange field is greater than that lost by the switching of spins, the material will have an intrinsic magnetization M even at 0 field and thus be considered a ferromagnet (not taking domains into account). Mathematically if $U\rho(E_f) \geq 1$ it is energetically favorable for the material to be a ferromagnet. This information is crucial as it implies that there is, what is referred to as, exchange splitting in ferromagnets [20]. The DOS of electrons antiparallel to M will be pushed upwards on the energy scale relative to parallel electrons as evident in Figure [5]. As discussed in Sub Chapter 2.1.3 DOS is a term present in the I(V) characteristics of tunnel barriers. As a result there will be spin polarized current in magnetic tunnel junctions.

2.3 The Completed Picture: MTJs and Tunneling Magnetoresistance

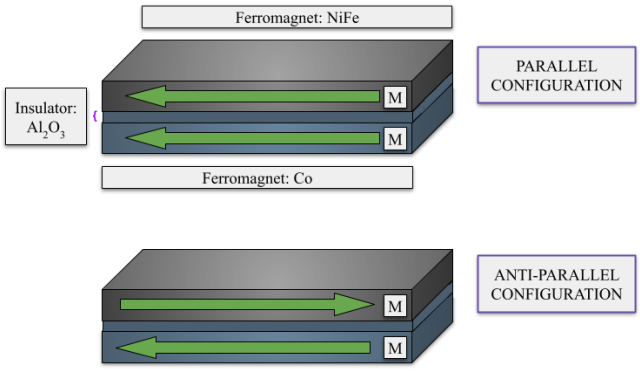

Figure 6: Diagram of a basic magnetic tunnel junction, the materials indicated are the one used in this thesis

In their most basic form magnetic tunnel junctions consist of two ferromagnetic electrodes separated by an insulating tunnel barrier as in Figure [6]. By using electrodes with different coercive fields it is possible to obtain parallel and anti parallel configurations as in Figure [6], the latter appearing when in between the two coercive fields. In this thesis the different coercive fields are obtained through the use of different electrode materials $Ni_{80}Fe_{20}$ and Co. What the previous sections built up to is that the spin splitting present in ferromagnets will cause a difference in densities of states at E_f, where most of the tunneling current comes from, resulting in spin polarized current across the barrier. Julliere in 1975 [1] was the first to observe such an effect, and also notice that parallel and anti parallel magnetization configurations yielded different values of conductance G (1/R). He formulated a simple model used to this day assuming no spin flipping during the tunneling process. As illustrated in Figure [7], the conductance of parallel and anti parallel configurations can be described as the sum of the contributions of majority and minority spin electrons at E_f in the left metal tunneling without spin flipping to states of the same spin in the right metal. It is important to notice from Figure [7] that if the MTJ is in the anti parallel configuration minority and majority spins will be reversed, hindering "up spin" current -and thus conductivity- by decreasing the number of available states at E_f in the right electrode. As a result parallel conductivity G_P will be greater than anti parallel conductivity G_{AP}. These individual contributions are then proportional to the number of electrons of the same spin on both sides of the barrier. This results in the following proportionalities for G (V=0):

$$G_P(V=0) \propto G_{MajMaj} + G_{MinMin} \propto aa' + (1-a)(1-a') \tag{16}$$

$$G_{AP}(V=0) \propto G_{MajMin} + G_{MinMaj} \propto a(1-a') + (1-a)a' \tag{17}$$

where a and a' are the fraction of atoms with moment parallel to the magnetization in the left and right electrodes respectively, making (1-a) and (1-a') those for moments anti parallel to M. Through this Julliere then defined the conductance variation as a function of the polarization of the two electrodes:

$$\frac{\Delta G}{G} = \frac{2PP'}{1+PP'} \tag{18}$$

for $P = 2a - 1$ and $P' = 2a' - 1$ [1]. The definition of spin polarization was refined throughout the years to include the influence of the tunnel barrier, obtaining the following result for tunneling spin polarization [10]:

$$P_{L,R} = \frac{\rho(E_{Fl/r})_{\uparrow}|M_{\uparrow}|^2 - \rho(E_{Fl/r})_{\downarrow}|M_{\downarrow}|^2}{\rho(E_{Fl/r})_{\uparrow}|M_{\uparrow}|^2 + \rho(E_{Fl/r})_{\downarrow}|M_{\downarrow}|^2} \tag{19}$$

Furthermore, it is now more common to use tunneling magnetoresistance as a measure of the difference between the two configurations defined as:

$$TMR = \frac{R_{AP} - R_P}{R_P} = \frac{2P_L P_R}{1 - P_L P_R} \tag{20}$$

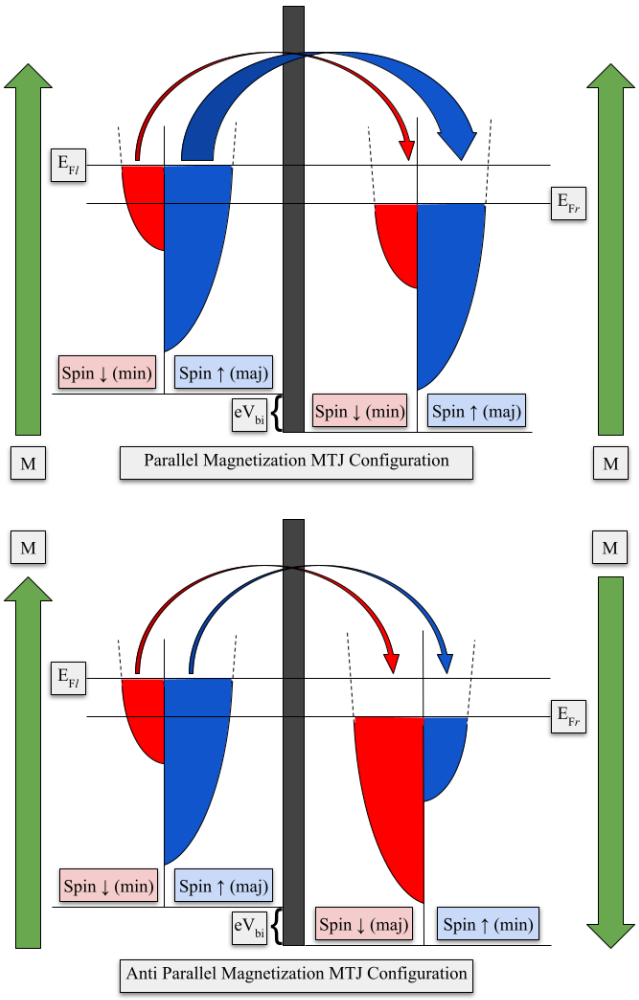

Figure 7: Visual representation of the Julliere model, helpful in visualizing the reason for the low and high resistance states of the MTJ. Adapted from a similar figure used in the author's Device physics assignment [21]

3 Experimental Setup

3.1 Fabrication Tools

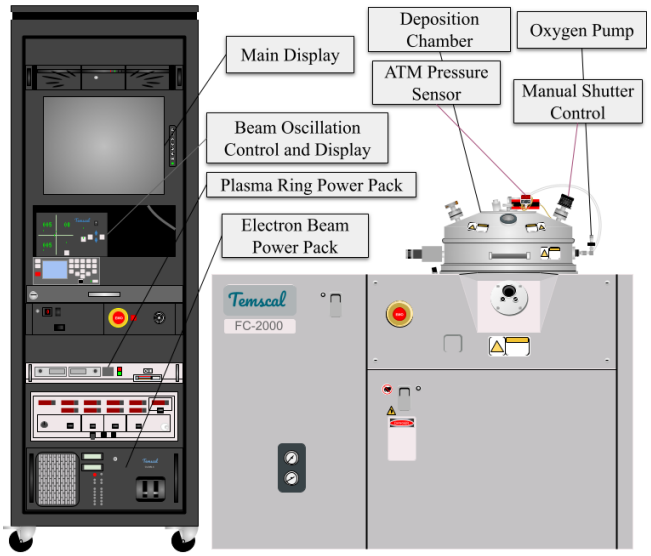

Figure 8: Figure showing a full outer view of the electron beam evaporation unit, the main fabrication tool used for this thesis

3.1.1 Electron Beam Evaporation

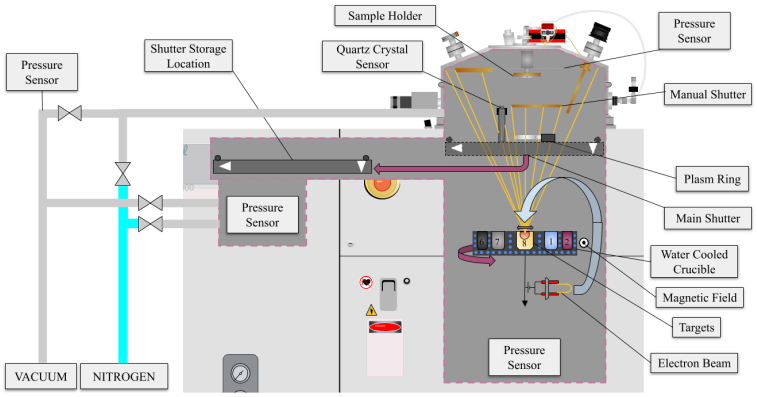

Figure 9: Figure displaying a full simplified view of the inner workings of the electron beam evaporator unit

All the devices fabricated during the course of this thesis were done so in a Temscal FC 2000 electron beam evaporation unit. The following description of electron beam deposition is mainly derived from Prof. Tamalika Banerjee's lecture notes on the subject in her nanoprobing and nanofabrication course, supplemented by other sources and my own experience with the machine. As detailed in Figure [9], the working principle of electron beam evaporators revolves around a thermionic or field emission activated electron gun below the target to be evaporated, curved by a magnetic field, making contact perpendicular to the target's surface. An essential step in the use of the electron beam evaporator is soaking. It consists of slowly incrementing the power of the beam followed by "soaking" periods of constant power, in this case, at 60 then 80%. The power and time details of this step must be included in the "recipe" given to the system along with the correct crucible number, evaporation rate and final thickness. It is crucial that the target be held in a water cooled, chemically inert and heat resistant crucible, to effectively dissipate heat without reacting with the target material. In addition, the whole system must be in high vacuum to prevent impurities and improve adhesion.

The target is then evaporated and will proceed to coat the entire chamber -as a point source to a first approximation [9]-, including the substrate placed above it, creating patterns with the use of photoresists or, in this case, shadow masks.

However, electron beam evaporators have many other features that improve deposition quality. Rather than being held stationary, the beam is rastered over the target surface to ensure uniform evaporation, maximize evaporation rate and control coating thickness uniformity [22], as well as avoid drilling a hole through the target and hitting the crucible directly. This can be observed in its dedicated display shown in Figure [8]. As hinted at previously, in the specific system used for this thesis the crucible holds up to 8 targets which can be rotated at will, each placed in their own holder coated in materials chemically inert to the specific target. The system used is also equipped with a quartz crystal sensor in the product chamber. Its purpose is to give real time information on the deposition rate and thickness to the user and the electron gun, the latter will stop once the desired thickness is reached. It does so by evaluating the dampening of the quartz' characteristic oscillation due to the weight of the deposited material. In addition to the main load lock separating the evaporation and product chambers, an additional manual shutter is used to allow the evaporation to reach the desired rate before beginning the deposition proper. Lastly a plasma ring was mounted in the product chamber, operated with a separate power source [8], with the purpose of plasma oxidizing the aluminum oxide tunnel barriers. As this is an essential part of fabrication it will be discussed separately in the following subsection. Temscal FC 2000 also has the possibility of temperature control with water coolant lines in the product chamber and heated stage [23]. In this case the substrate was kept at room temperature to avoid intermixing of layers and obtain a smooth tunneling interface. It is precisely for this reason that electron beam evaporation was chosen as, with it's gentler deposition compared to sputtering, it was possible to at least minimize the intermixing of layers through more favorable kinetics of the deposition; a precaution LeClair strongly advocated for in his thesis [10].

3.1.2 Plasma Oxidation

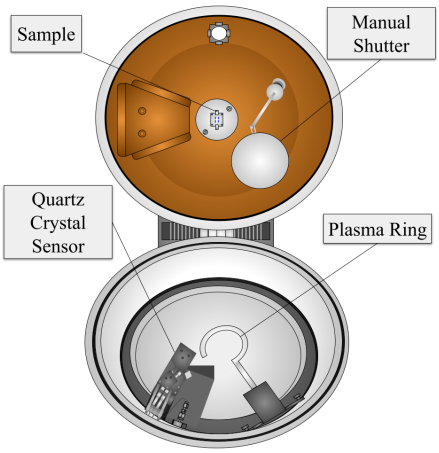

Figure 10: Figure displaying the product chamber and plasma ring layout

To obtain the oxygen plasma required to further oxidize the Al_2O_3 layers, an aluminum plasma ring was mounted in the product chamber as per Figure [10]. The ring itself will simply act as a cathode as current from its power source shown in Figure [8] passes through it. The chamber itself is purged using oxygen and then placed at an oxygen pressure of 0.1 T via the oxygen intake pictured in Figure [9]. The strong electric field will attract the positively charged oxygen nuclei and repel the negatively charged electrons, resulting in some free electrons. These free electrons will then be accelerated by the field and will collide with the other oxygen atoms, creating more free electrons and ions and, through a chain reaction, oxygen plasma [24]. The plasma won't simply contain positive oxygen ions; molecular oxygen O_2, atomic oxygen O, negative oxygen ions O^{2-} as well as free electrons make up the plasma. It is in fact most likely atomic oxygen that will react with the surface atoms of the sample and oxidize it [25]. One of the advantages of plasma oxidation is that the ions and free electrons present in the plasma will aid the reaction, increasing its rate. Another advantage of plasma oxidation is that it is

a dry process, avoiding contamination from the fluids used in wet oxidation processes. Furthermore it can be carried out at much lower temperatures than thermal oxidation, reducing the risk of heat generated defects [25]. Unfortunately the system used in this thesis does have some faults. Being a hook rather than ring shape the plasma formation is anisotropic and appears visible mainly in the bottom left of the chamber, corresponding to the empty region of the hook.

3.2 Characterization Apparatuses

3.2.1 Keysight + Manual Probe Station

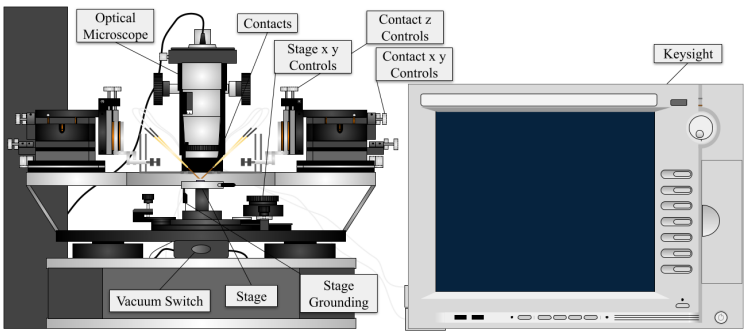

Figure 11: Figure displaying the Keysight and probe station setup

The combination of a keysight B1500A device parameter analyzer and Cascade Microtech manual probe station was mainly utilized in this thesis as a preliminary I-V characterization tool. This was done by selecting the I-V sweep standard test program and inputting the desired voltage range, step number and compliance -maximum current allowed to flow through the circuit-. For the safety of the machine and samples it is necessary to always wear a grounding bracelet when performing tests and to only lightly touch the surface with the probes. Furthermore it was used to check the quality of the tunnel barrier oxidation by measuring the planar I-V characteristics of the oxide layer and comparing it with known resistance profiles of aluminum oxide. It was also used to test the isolation of the top and bottom contacts in the tunnel barriers by comparing the I-V characteristics of both individually with those of the whole tunnel barrier. This allowed the discarding of faulty devices before more time than necessary was spent on their characterization with the following more advanced systems.

3.2.2 Temperature and Magnetic Field Measurements: the ”Bloch” Setup

For the purposes of this thesis the setup pictured in Figure [13], named ”Bloch” within the faculty, offered the ability to perform I-V characteristics measurements at various temperatures and under a magnetic field of varying strength. In addition, to observe TMR it was also possible to measure the current through the devices while sweeping through a range of magnetic field strengths at a set voltage. To achieve a precise control of temperature, liquid nitrogen is used to cool down the samples. Held in a reservoir, the nitrogen is forced to the sample chamber via a vacuum pump which creates a difference in pressure between the two end of the transfer tube. This pressure difference, and thus the rate of nitrogen flow is controlled by an instrument named Mercury which also controls a heating unit behind the sample, allowing it to reach a temperature set by the operator. The sample is also placed in high vacuum via a separate vacuum pump to prevent any environmental factors from tampering with the sample such as in air oxidation. Lastly the sample holder is placed in between two rotatable toroidal coils which generate a magnetic field along the central axis joining them which in this case would be in plane with the sample. This magnetic field is controlled by the power source of the toroidal coils, which allows for the selection of the current that flows through the coils and thus, via

a known conversion factor of 16.09375 mT/A, a specific field magnitude. Both current and voltage sourcing is possible via a

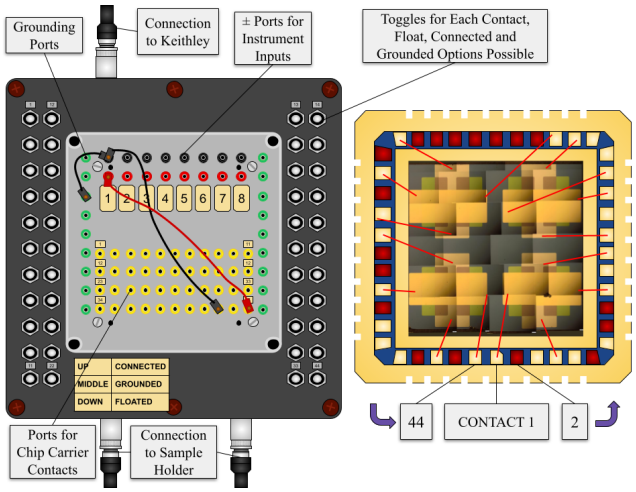

Figure 12: Figure displaying the wire box setup for ”Bloch” as well as the chip carrier. It is displaying a 2 probe measurement of Device 4.

Keithley 2401 source meter. Through this instrument both 2 probe and 4 probe measurements are possible. The 4 probe configuration has a higher accuracy, the details of which can be found in [26]. By feeding a control sequence to the system in charge of all the instruments it is also possible to perform sweeps over temperature and magnetic field magnitude, the latter of which was used to observe the TMR effect. The samples were held in a chip carrier and wire bonded as per Figure [12]. Each contact on the chip carrier corresponds to a port in the wire box, each contact can be connected, grounded or floated via the switches on the sides of said wire box. The wire box is connected to the Keithley and the sample holder.

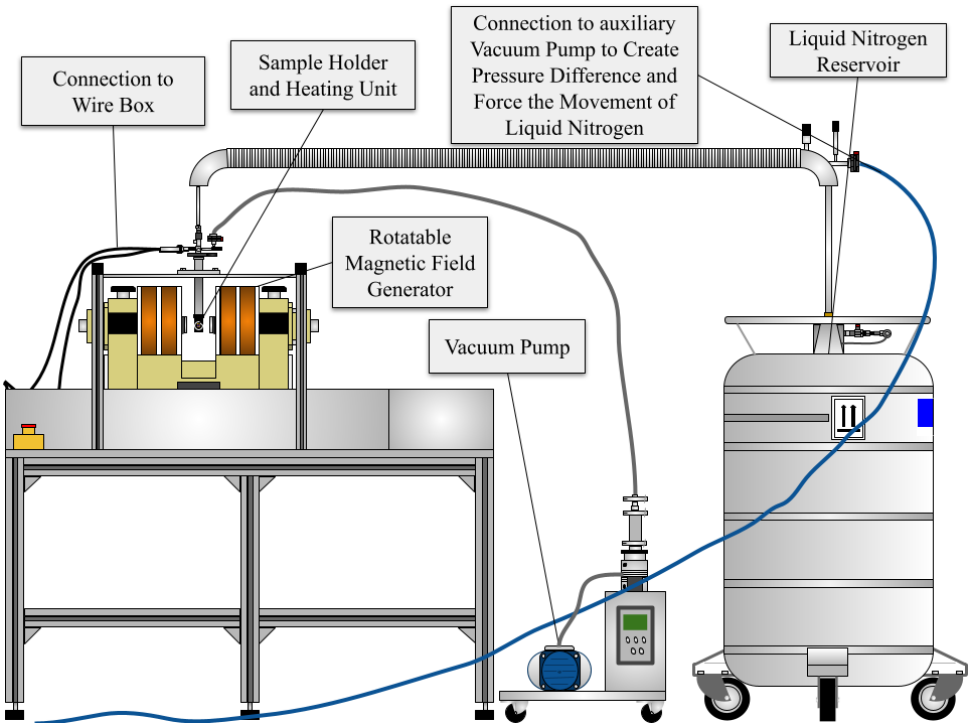

Figure 13: Figure displaying the ”Bloch” setup capable of Temperature and magnetic field dependent current measurements. The figure omits the tower housing the control centers for each instrument as the focus of the section will be on the instruments themselves.

4 Methods

4.1 Tunnel Junction Fabrication

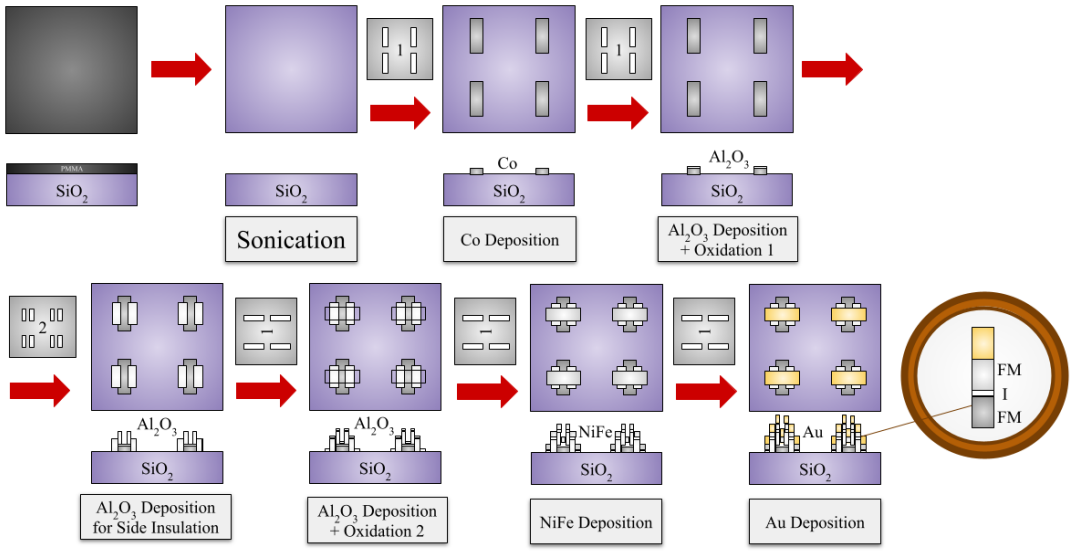

Figure 14: Figure detailing the fabrication process of the $Co/Al_2O_3/Ni_{80}Fe_{20}/Au$ tunnel junction

A total of 8 depositions were completed to obtain a final working sample each containing 4 magnetic tunnel junctions referred to as devices 1 through 4 beginning at the bottom right and moving counterclockwise. All fabrications were performed using the Temescal electron beam evaporator who's function is described in detail in Sub Chapter [3.1.1]. The first deposition consisted of 30 nm of cobalt deposited directly onto a SiO_2 substrate and covered with 4 nm of Al_2O_3 further plasma oxidized for 5:30 minutes to rid it of non oxidized aluminum pockets which facilitate spin independent conduction. This was done with the aim of testing the degree of plasma oxidation of the samples in the available setup described in Sub Chapter [3.1.2]. All remaining depositions aside from the seventh used the same general process for obtaining cross bar geometry tunnel junctions described in the following paragraph, the only differences are the electrode materials and thicknesses as well as Al_2O_3 thickness and oxidation time. Samples two and three consisted of 30 nm gold electrodes with 3 nm Al_2O_3 tunnel barriers oxidized for a total of 6 minutes. Sample four replaced the bottom gold electrode with 35 nm of cobalt and the top electrode with 5 nm of $Ni_{80}Fe_{20}$ and 35 nm of gold, as well as increased the thickness and oxidation time of the Al_2O_3 to a total of 4 nm and 12 minutes, whereas in samples five and six Al_2O_3 was only oxidized for 11 minutes. Sample eight was very similar, however opting for 30 nm of $Ni_{80}Fe_{20}$ and 2 nm of Al_2O_3 oxidized for 3 minutes. Sample seven was yet another test of the degree of oxidation of the samples and consisted of the same general design as sample one, but with four gold pads on top of it deposited through shadow mask 2 shown in Figure [14] and a 2 nm Al_2O_3 layer oxidized for 4 minutes for half of the sample and 5 minutes for the other half. The following paragraph will detail the fabrication of the crossbar formation samples through that of sample eight as it is the final working magnetic tunnel junction sample on which most of the results and discussion section is based. It is easy to extrapolate this method to the other tunnel junction stacks described.

To imprint patterns on the substrate, shadow masks like the ones pictured in Figure [14] were used rather than a photo-lithographic method to avoid contamination from photoresists and solvents as

well as speed up the fabrication process. The following recount of the process can be made more comprehensible by following the visual aid of Figure [14]. All masks and components of the plasma ring were cleaned thoroughly with acetone and isopropanol, while the substrate's protective PMMA layer was removed through power 9 sonication for 5 minutes. The substrate was mounted onto the chuck, covered with the first shadow-mask in a vertical orientation and placed in the product chamber. A recipe for the first Co layer deposition was uploaded, detailing the desired material crucible number, 35 nm thickness, 1 Å/s rate and the power goal for the first and second soaking steps, as well as soaking and rise times. In order to ensure a growth under the constant, desired, deposition rate 40 nm were requested and the manual shutter was kept closed for the first 5 nm of the growth. Once the process is started the system balances the pressure in product and evaporation chambers, reaching a high vacuum of $4 \cdot 10^{-6}$ Torr and opens the chamber separation shutter. After which it begins the rise and soak process and the target starts to evaporate. Once 5 nm are deposited and the deposition reached the required rate -both observed using a built in quartz crystal sensor- the manual shutter is opened and the deposition is allowed to take its course. In most cases the target thickness is overshot by 1-3 nm thus the manual shutter was once again closed as the desired thickness is reached. By the same process, without changing mask or opening the chamber, a 1 nm layer of Al_2O_3 is deposited. The target thickness inputted was 6 nm, the rate 0.4 Å/s and the pressure $6 \cdot 10^{-6}$ Torr - although by this time it reached the E-7 Torr range - as the uniformity of barrier growth is essential for a successful tunnel junction fabrication. As already hinted at, further oxidation via oxygen plasma is required to purge the Al_2O_3 of any aluminum pockets through which current can flow avoiding tunneling. To achieve this the product chamber is sealed and purged thrice using oxygen, reaching a pressure of 5 Torr, then removing it via vacuum pump, achieving $2.5 \cdot 10^{-2}$ Torr. The chamber is then inundated with oxygen to a pressure of 0.1 Torr and the ring is turned on with a voltage of 0.3 kV and a current of 200 mA. The oxidation, detailed in section [3.1.2] is allowed to continue for 1:30 minutes. The chamber is then opened and the second mask used in place of the first, still in a vertical orientation. 50 nm of Al_2O_3 used for insulation is deposited at a rate of 1.5 Å/s. The first mask is placed back on top of the sample, however in a perpendicular orientation to form a "cross bar" geometry. The reverse process is now performed, first growing a 1 nm Al_2O_3 layer and oxidizing it for 1:30 minutes, then depositing 30 nm of $Ni_{80}Fe_{20}$ at a rate of 1 Å/s followed by 30 nm of Au deposited at 2 Å/s. The resulting sample is pictured below [15].

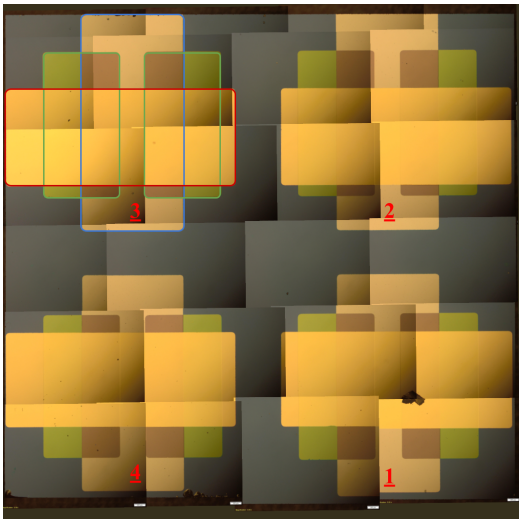

Figure 15: Image of working MTJ sample (8) obtained by stitching snapshots of optical microscope scans. The devices are labeled with numbers as they appear in characterization tests

4.2 Characterization Methods

4.2.1 General M/I/M Characterization

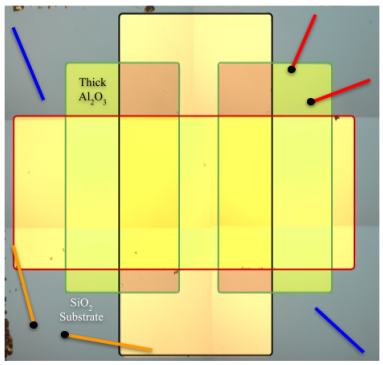

(a) Figure showing the keysight probe configurations for the sanity checks performed on each sample, the black circles at the end of the probes represent contact, the different colors represent different tests

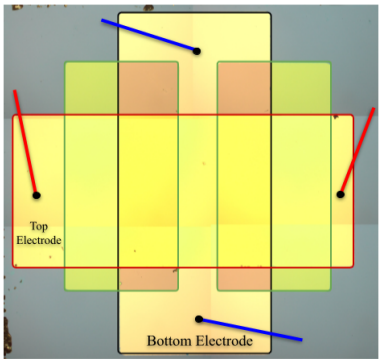

(b) Figure representing Keysight probe configurations for the tests ran on the top and bottom electrodes

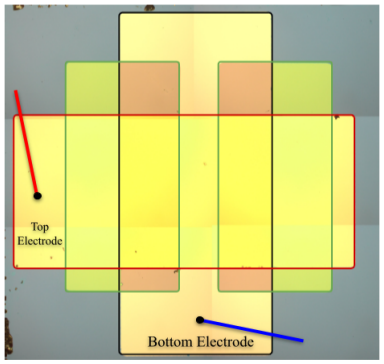

(c) Figure representing Keysight probe configuration for the tests ran on the full junction

Figure 16: Figures portraying the Keysight electrode configurations for the standard tests ran on all samples and devices

Preliminary I-V Characteristics Checks: All the devices fabricated for this thesis had their I-V characteristics preemptively checked for tunneling features using the keysight instrument detailed in Subchapter [3.2.1]. All the probe positions are displayed in Figure [16] as to make it easier to follow the subsequent explanation. For the following tests the voltage range was set to $\pm 10mV$ and the compliance to $10\mu A$ so as to not damage the devices. Initial sanity checks were performed on the open circuit, SiO_2 substrate and thick Al_2O_3 layers as shown in Figure [16a] to ensure that they all indeed behaved as insulators. The top and bottom electrodes of each device were then probed as in Figure [16b], ideally expecting to observe clear metal behavior -low resistance and a quick rise to compliance -. If the probes are placed lightly enough on the bottom electrode it could be expected to see some tunneling behavior as in all cases it is covered by a thin Al_2O_3 tunnel barrier. Finally the I-V characteristics of every barrier are probed in the configuration shown in Figure [16c]. In order to observe up to the cubic "intermediate voltage" regime expected by the Simmons model, multiple measurements were taken with increasing voltage range from $\pm 10mV$ to $\pm 150mV$ in steps of $20mV$. The expected outcome is a non symmetric linear I-V trend, transitioning to a non symmetric cubic I-V trend. Further non systematic tests were performed to explain unexpected trends in the data. These will be briefly described in the discussion section where relevant.

Temperature Dependence of I-V Characteristics: Keeping the same contact configuration as in Figure [16c], however by wire bonding the sample to a chip carrier as in Figure [12] it was possible to obtain temperature dependent I-V sweeps for sample six using the "Bloch" setup described in Subchapter [3.2.2]. Unfortunately only devices 1 and 3 were successfully wire bonded due to multiple shorted contacts in the wire box (highlighted in red in Figure [12]). All four contacts of each device

were wire bonded to allow for 4 probe measurements, however both 2 probe and 4 probe configurations were tested with no discernible difference. The extra accuracy of 4 probe testing -the origin of which is described well in [26]- becomes more valuable in the much more sensitive TMR measurements. The sample was loaded onto the sample holder of the Bloch setup which was allowed to reach a vacuum of $1.3 \cdot 10^{-6}$ Torr. Additionally it was connected to the liquid nitrogen reservoir used to lower its temperature. Through the Keithley instrument an initial set of I-Vs ranging from $\pm 10mV$ to $\pm 100mV$ -where the cubic regime was first clearly observable- for both devices were taken at the room temperature of 293 K. Having confirmed that in the potential range of $\pm 100mV$ the devices are safe and show tunneling characteristics, the temperature was allowed to decrease and settle to 200 K through the Mercury instrument. I-V characteristics for both devices were recorded for $\pm 100mV$, after which the process was repeated for 180 K, 160 K and 130 K. This data was then fit using the simmons model, the code for which can be found in Appendix [B].

4.2.2 MTJ Characterization

Bias voltage dependence of TMR: Sample eight was the only one to show a TMR thus the following characterization method pertains to it. The sample was mounted in the Bloch set up and cooled down to the lowest temperature achievable using liquid nitrogen 75 K. Connecting the electrodes in a four probe configuration with the gold contact as the positive end and the cobalt contact as the negative end an I-V sweep was ran, increasing the potential range until clear non linearity was observed at 55 mV. Consequently, current output vs current supplied to the coil - and thus magnetic field - sweeps of device 2 were ran at 15 mV (where the current still appeared in the linear regime), 25 mV, 35 mV, 45 mV and 55 mV. To then translate this data into what is shown in Graph [19a] the current supplied to the coils was multiplied by 16.09375, the linear scaling factor between it and the magnetic field in mT. The resistances were then obtained from the current data by dividing the set potential by them, after which they were normalized with respect to the parallel resistance state. The code used for this can be seen in Appendix [B]. Due to time concerns and wanting to safeguard our best device (4) this was performed exclusively for device 2.

Temperature dependence of TMR: It was opted for 15 mV as the constant bias of choice for the following tests as any lower and noise makes it difficult to discern the TMR, whereas any higher and the bias voltage dependency would significantly decrease its value, making it harder to observe it at higher temperatures. As device 2 showed a discrepancy at zero field it was opted to perform the temperature dependent measurements on device 4. Using the same contact configuration as for the bias voltage dependent measurements, and beginning from 75 K, the same output current vs magnetic field sweep was recorded. The same was done for 100 K, 125 K, 150 K, 200 K, 250 K and 300 K. Unfortunately, due to time concerns the sample was not allowed to completely settle at the aforementioned temperatures. As such, as the 6 minute measurement took its course the sample continued to heat up leading to lower resistances and thus higher currents at the end of the sweep than at the beginning as shown in the individual temperature graphs in Appendix [A]. It was confirmed that this was indeed the cause as another measurement was taken the morning after at room temperature (293 K), and lacked this feature as expected. The current difference was also found to be roughly the same for all temperatures, thus making it more pronounced in low TMR Graphs [23]. This was the reason as to why Figure [20a] only displays 75 K, 100 K and 293 K.

5 Results and Discussion

While the goals of observing the bias and temperature dependency of TMR, as well as temperature dependency of the I-V characteristics of MIM tunnel barriers, were reached, many interesting phenomena were explored through the trial and error that led up to the final fabrication. It is thus appropriate to recount and discuss the results in the order of the samples from which they were obtained. In addition this will aid in following the thought process behind the conclusions drawn.

5.1 Temperature Dependent I-V Characteristics of Regular MIM Tunnel Junctions

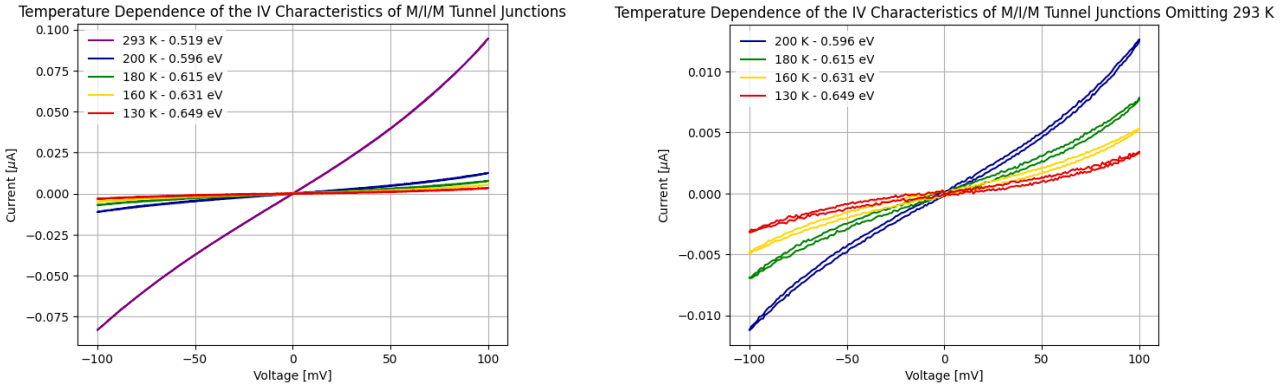

(a) Full range of temperature dependent tunneling I-V characteristics. Fitted barrier heights are included in the Legend.

(b) Clearer depiction of temperature dependent tunneling I-V characteristics obtained by removing the 293 K line. Fitted barrier heights are included in the Legend.

Figure 17: Graphs portraying the temperature dependence of tunnel barrier I-V characteristics

The previously described samples two and three, consisting of four $Au/Al_2O_3/Au$ M/I/M devices, failed to exhibit the I-V characteristics expected by the Simmons model, instead appearing shorted, quickly reaching compliance as would be expected if the two gold electrodes were in contact. There are two possible physical explanations for this behavior. The presence of a shadow mask not in perfect physical contact with the substrate, causes the deposited pattern to have tapered edges and thus become larger than the intended area by a factor $E = 1 + c/d$ where d is the source to mask distance and c is the mask-substrate separation [27]. This could have caused the top and bottom electrodes to touch leading to the observed shorting behavior. Consequently AFM imaging of all significant pattern edges was done one example of which can be seen in Figure [18]. As on the ends of the electrodes this penumbra effect did not extend past the 50 nm aluminum oxide isolation barriers, and in the center the bottom electrode is shielded by 1.5 nm of aluminum oxide, this explanation for the shorting behavior can be ruled out. The answer must then lie in the formation of the tunnel barrier itself, and, with the added knowledge that the following samples consisting of $Co/Al_2O_3/Ni_{80}Fe_{20}$ - oxidized both more and less than samples two and three - did not run into this issue, it can likely be attributed to the gold electrodes. While 5 μm by 5 μm atomic force microscopy (AFM) imaging was performed on the surface of both bottom gold and cobalt electrodes, concluding that both had reasonable rms roughness values of around 0.6 nm, the use of gold can still affect pinhole formation. Unlike cobalt, gold is inert and does not form oxides, meaning that any insulating electrode-oxide layer formed by excess plasma oxidation, that could have helped obstruct pinhole conduction, would not be present. In an attempt to

overcome this shorting issue inherent to the tunnel barrier, the aforementioned samples four, five and six were fabricated, all with thicker 4 nm oxide barriers and longer oxidation times up to 12 min.

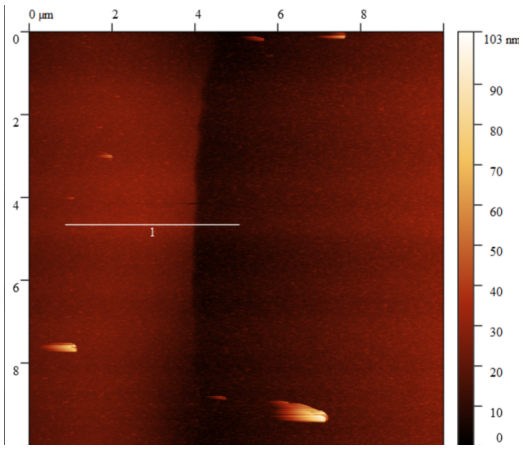

(a) AFM image of the surface shown in the figure to the right

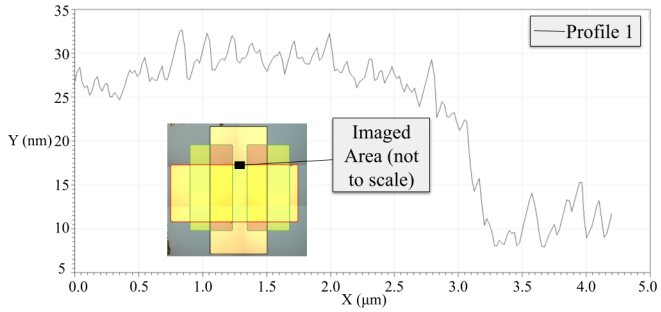

(b) profile of the step imaged by the AFM showing a slight tapering of the edge of the deposited electrode

Figure 18: An example of the AFM imaging done on the edges of the deposited patterns showing slight tapering of the electrode edge at the center of the device

The temperature dependent I-V characteristics visible in Figure [17] originate from device 3 of sample six. As mentioned in Subchapter [2.1.2] the Simmons model expects a linear regime at low bias voltage, transitioning to a cubic regime and then an exponential region. Figure [17] exhibits up to the cubic regime as well as an expected slight asymmetry due to the differing work functions of cobalt and $Ni_{80}Fe_{20}$. This specific device is interesting as it also showed a slight hysteresis increasing with a decrease in temperature; most likely due to defects in the barrier creating trapping states which are filled upon the application of forward bias and discharged in reverse bias [28]. The temperature dependence of the I-V characteristics itself is clearly observable, as the temperature was reduced the devices became increasingly resistive. To put a number to this qualitative statement, at 5 mV, well within the linear regime, the resistance increases from 1.34 $M\Omega$ at 293 K to 43.2 $M\Omega$ at 130 K. When straying further from Simmons' approximations it becomes evident that conduction across the tunnel barrier includes multiple mechanisms other than direct tunneling, some of which temperature dependent. Citation [29] provides a comprehensive list of all of these effects. Thanks to the large barrier heights in comparison to the voltage and temperature ranges tested, the contribution of mechanisms such as Fowler-Nordheim Tunneling -where at high applied potentials the tunneling electron will face the thinner triangular region of the barrier- and thermionic emission -where electrons have enough thermal energy to overcome the tunnel barrier altogether- can be safely considered negligible. To begin, direct conduction is in itself somewhat temperature dependent. At 0 K, as assumed by Simmons when solving the current density integral, the Fermi-Dirac distribution is a step function with its precipice at the Fermi Energy of the material. However, as the temperature increases, the Fermi-Dirac distribution spreads [9], allowing electrons access to states of higher energies, facing a lower effective tunnel barrier and thus achieving greater tunneling probabilities. As this spreading increases with temperature, so does the number of electrons capable of conduction, thus increasing current. Another relevant mode of transport across the barrier described in [29] is "hopping conduction" otherwise known as trap assisted tunneling. Imperfect tunnel barriers harbor trap states of different energies and positions in the barrier. These states provide a current path where the electron can perform multiple

tunneling steps with distance [a] between trap states << d where in between each step it can be aided thermally or by phonon absorption. Current density due to this process follows the following relation:

$$J = qan\nu \cdot exp(\frac{qaE}{k_bT} - \frac{E_a}{k_bT}) \tag{21}$$

Where E is the applied electric field -in this case V_B/d-, n is the trap density, ν is the frequency of tunneling attempts and E_a is the energy difference between trap state and conduction state of the insulator. In the case of this device, where qaV/d $< E_a$ for any a < and nonphysical 80 nm (assuming $E_a \approx \bar{\phi}$), this conduction pathway introduces an exp(-1/T) relationship to the current across the tunnel junction. This most likely contributing to the non linear decrease in Resistance with T observed in Figures [17]. It is also worth mentioning that part of this T dependence may also result from the thermal spread of the Fermi-Dirac distribution making higher energy trap states available. Higher temperatures also lead to greater excitations of phonons within the barrier and magnons -quantized spin waves- at the insulator/ferromagnet interfaces which can assist tunneling and thus decrease resistance [30]. To avoid repetition a deeper explanation of this phenomenon will be given in the following paragraphs where it is more relevant. As previously discussed, the Simmons model assumes 0 K and disregards the effect of trap states and pinholes, only focusing on pure tunneling current. In doing so it becomes a perfect instrument for determining the quality of tunnel barrier deposition. By keeping the barrier area and width constant at the experimental values of 853 μm^2 and 4 nm respectively, and allowing for the fitting of only barrier height, the values presented in Figure [17a] were obtained and three conclusions can be drawn. Firstly, although their absolute values can't be trusted as the empirical values of barrier thickness and area could not be collected, and they will continue to marginally decrease as 0 K is approached, this first approximation shows a significantly lower barrier height than the theoretical average for this junction of 2 eV (see Appendix [C]). Consequently, current across the junction is greater than expected which, along with the rms roughness values collected, highlights the non-uniformity of barrier growth achieved, likely containing numerous pinholes and trap states. Furthermore, it also hints at low if not absent cobalt oxide formation despite the long plasma oxidation time.

5.2 Bias Dependency of TMR

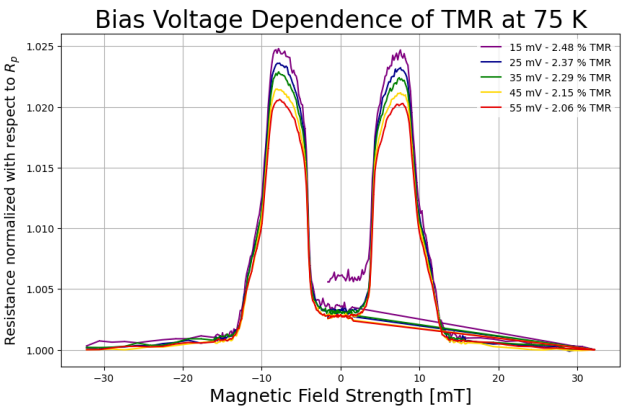

(a) Graph highlighting the decrease in TMR sample eight's device two with increasing bias voltage

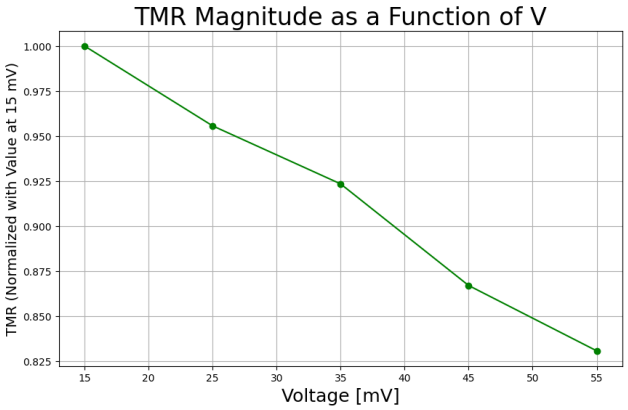

(b) graph showing a nearly linear dependence of TMR on bias voltage observed in the data collected

Figure 19: Graphs showing the bias voltage dependence of TMR

Being composed of ferromagnetic electrodes, device six was also tested for TMR by performing a magnetic field sweep at various potentials, however none was observed. Possible reasons for this lack of MTJ behavior include the $Ni_{80}Fe_{20}$ layer being too thin. Ordered magnetization in thin film nickel has been observed to nearly vanish by 2.8 nm, already showing a significant decrease compared to bulk by 6 nm. This was attributed to more pronounced island like Volmer-Weber growth as thickness decreases [31], which would make exchange interactions throughout the layer weaker, disrupting ordered magnetization. As nickel is generally the prevalent element in permalloy and the growth method used in this report has been shown to be severely non-uniform, it is possible that a 5 nm layer of $Ni_{80}Fe_{20}$ did not act as a ferromagnet in this geometry, impeding TMR. Furthermore the substantial tunnel barrier thickness of sample six resulted in the aforementioned large resistance values. As TMR is the weighted difference of the two resistance states, as shown in Equation [20], when tunnel barrier thickness increases both parallel and anti parallel resistances will increase exponentially, keeping the numerator relatively unchanged but greatly increasing the denominator, effectively extinguishing the TMR. Both of these issues were tackled in sample eight by increasing $Ni_{80}Fe_{20}$ thickness to 30 nm, decreasing the barrier thickness to 2 nm and the oxidation time with it to 3 minutes total.

There was clearly merit to this reasoning as all devices of sample eight displayed a TMR. Graphed in Figure [19] is the bias voltage dependence of device two's TMR at 75 K. What stands out at first from these results is the low TMR of 2.48 %. In fact if Julliere's TMR definition [20] is to be followed, by taking spin polarization values for cobalt and $Ni_{80}Fe_{20}$ from literature, 42 % [32] and 35 % [33] respectively, the TMR for this junction should be in the vicinity of 35 %. The answer to this might lie in the resistance values observed in these devices, ranging from 678 Ω for device two, to 1141 Ω for device four, being much lower than the 220 $k\Omega$ expected by a quick Simmons model calculation (using ideal parameters such as 2 eV barrier height, 2 nm barrier width and 853 μm^2 at the same bias the other resistances were taken; the code for which is shown in Appendix [B]). This decrease in resistance results from the incorporation of the previously discussed spin independent conductance paths such as from pinholes, trap states and phonon assisted tunneling which, for such a discrepancy between the ideal and observed resistances, must be plentiful. If one takes for instance a device where all current is from direct tunneling, the high resistance state has a resistance of 100 Ω and the low resistance state has a resistance of 1 Ω, the TMR according to Equation [20] will be 9800 %. Now if a new path is added which facilitates conductance regardless of the original spin of the electron, a path of resistance say 1 Ω will be appear in both AP and P configurations; by modeling this scenario as two resistors in parallel the new R_{AP} will be 0.99 Ω and R_P will be 0.5 Ω leading to a TMR of 98 %. Magnon assisted tunneling will also cause spin flipping during transport, more directly decreasing TMR, this will however be explained in more detail in the following paragraphs. Xi Chen and R. H. Victora's work on theoretically modeling the "Effect of Pinholes in Magnetic Tunnel Junctions" does an excellent job explaining another important mechanism which impacts TMR values [34]. By modeling pinholes as a 1 atom wide ferromagnetic "tunnel" connecting the two electrodes through the barrier with a sharp domain wall in between, they were able to calculate its impact on the device's conductance as a function of electron energy. They showed that, due to the confinement of the electron wave functions in this "tunnel" structure, the energy levels of electrons in the structure will be discrete and within the conduction band of the electrodes so that, when the energy of an electron matches that of one of the confined states, it will perform "resonant tunneling". When averaged over many pinholes of different shapes, modeling a non uniform tunnel barrier such as in the fabricated samples, it was shown that it results in an almost ohmic current and a much lower TMR than expected for a perfect MTJ. This is due to many more electrons of different energies being capable of tunneling thus reducing spin polarization. Other mechanisms could cause a lowering of the TMR, such as the

presence of antiferromagnetic cobalt oxide formed during the plasma oxidation which, having no spin polarization, can strongly affect the effective spin polarization "felt" by the tunnel barrier and even completely overcome that of the electrode if thicker than 5 monolayers [10].

Nevertheless a TMR was achieved in these devices and, as is the main focus of Figure [19a], it was observed to decrease with increasing applied bias voltage. This decrease is common to all MTJ devices in literature regardless of the quality of the tunnel barrier. The issue must therefore be intrinsic to magnetic tunnel junctions themselves. It has been proven by S. O. Valenzuela et.al. through experiments on $Al/Al_2O_3/FM$ junctions, that as the bias voltage increases the spin polarization of a ferromagnet that is the origin of the tunneling electron will decrease slightly, while that of the ferromagnet receiving the electron will decrease dramatically [35]. They attribute this result to the idea that, at low bias, electrons tunnel from energy levels near the Fermi level of the first ferromagnet, where spin polarization is high, into energy levels in a similar range in the second ferromagnet where spin polarization is, likewise, high (see Figure [5]). On the other hand, the shift in Fermi levels introduced at higher bias voltage does not affect the energy level of origin of the electron, but causes it to tunnel into states of higher energy they refer to as "hot", where spin polarization is lower and will continue to decrease as the bias voltage is increased. While corroborating this theory by modeling their devices assuming both electrodes to be free electron potentials, the barrier to be rectangular and no spin flipping, they ran into the same curious discrepancy at low voltages as many other publications at the time. What is referred to as "zero bias anomaly" is a region below roughly 200 mV where at low temperatures the parallel and anti parallel resistances as well as TMR seem to show an abnormal proportionality to bias. It was considered an anomaly because at such low bias, where difference in spin polarization is small, R_P, R_{AP} and by extension TMR should be roughly constant as expected from taking the derivative of the Simmons model at low bias (I roughly linear with V). As expected this discrepancy was observed in the collected data -pictured in Figure [19b] as a clearly non constant but rather linearly decreasing TMR with V- as it was taken in a range of 15 mV to 55 mV, well below the 200 mV edge of the "zero bias anomaly". As such it is important to understand what causes this effect. An unfortunate shortcoming of both the Simmons and Julliere models is that they consider solely direct tunneling. In 1997 S. Zhang and P. M. Levy [36] developed a theoretical model based on including the effect of magnon excitations at the FM/I interfaces on tunneling current with the goal of explaining the "zero bias anomaly". They proposed that the energy difference between tunneling electrons and the Fermi level of the acceptor ferromagnet caused by the bias voltage, forces them to lower their energy by producing a magnon of equal energy. The model equation they derived from this intuition showed that both G_P, G_{AP} appear to have a linear dependence on bias voltage in a term associated with inelastic magnon assisted transport. Furthermore the anti parallel state's linear dependence appears to be steeper as V is multiplied by $(\alpha\rho_L^{min}\rho_R^{min} + \beta\rho_L^{maj}\rho_R^{maj})$ whereas in the parallel state V is multiplied by $(\gamma\rho_L^{min}\rho_R^{maj})$ -where α, β and γ are constants irrelevant to this discussion- thus the anti parallel resistance will decrease faster than the parallel resistance with V leading to a lower TMR as V increases. Recalling Julliere's model or looking at the relevant term in S. Zhang and P. M. Levy, this DOS dependence is the opposite of what is expected in direct tunneling. This is paralleled in the physics of magnon assisted tunneling. Magnons are spin wave quanta which correspond to a spin of -1, thus when a spin down electron tunnels through the barrier and releases a magnon it must flip to spin up to conserve spin and will thus settle in a spin up state. Conversely when a spin up electron absorbs a magnon it must flip to spin down [37], the opposite processes are not possible due to spin conservation. In the parallel state this will cause majority electrons to tunnel into minority spins and vice versa, leading to a more inefficient transport process analogous to the anti parallel state in the Julliere model, and the opposite will be true for magnon spin flip tunneling in the

anti parallel configuration, bringing the resistances of these two additional pathways closer together and thus decreasing TMR. The general TMR dependence on bias voltage can be approximated by simplifying S. Zhang and P. M. Levy's equations for G_P, G_{AP} as:

$$G_P = G_{0P} + AV$$
$$G_{AP} = G_{0AP} + BV$$

where G_{0P} and G_{0AP} are the non bias voltage dependent terms such as direct tunneling and A and B are the aforementioned coefficients of the bias voltage dependence. Substituting these expressions into the equation for TMR [20] :

$$TMR = \frac{G_P - G_{AP}}{G_{AP}} = \frac{G_{0P} - G_{0AP} + (A-B)V}{G_{0AP} + BV} = \frac{a + bV}{G_{0AP} + BV} \tag{22}$$

as explained previously A < B, thus $b < 0$, on the other hand, due to Julliere model considerations $G_P > G_{AP}$ and therefore $a > 0$. The range of tested bias voltages fits within a low bias approximation where $G_{0AP} >> BV$, and therefore the equation for TMR can be written as:

$$TMR = \frac{a}{G_{0AP}} + \frac{b}{G_{0AP}}V \tag{23}$$

thus explaining the linearly decreasing trend in TMR vs V observed in Figure [19b]. This regime of the TMR-bias characteristics is also contained below the maximum energy of magnons in the electrodes $E_{max} = 3k_B T_c/(S+1)$, where T_c is the Curie temperature and S is the ferromagnet's spin, giving further validity to this explanation of the "zero bias anomaly" [10]. By S. Zhang and P. M. Levy's own admission this model does not fully explain the trends observed experimentally suggesting more factors must play a role.

5.3 Temperature Dependency of TMR

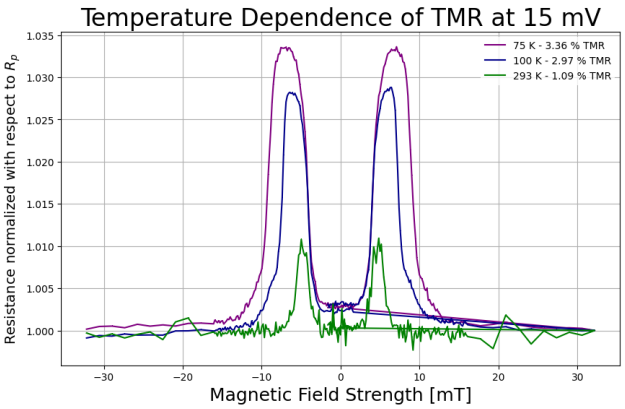

(a) Graph depicting the decrease in TMR with increase in temperature

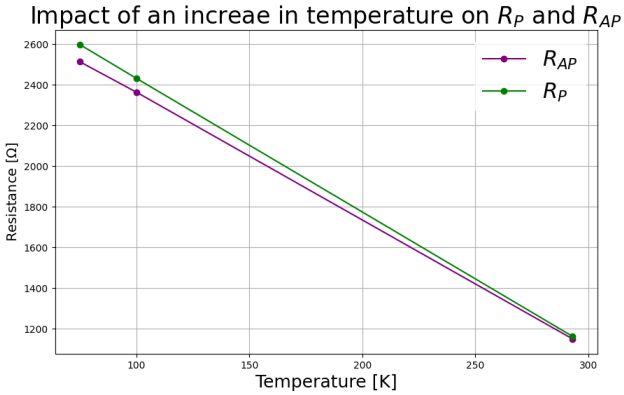

(b) Graph showing separately the decreases of parallel and anti parallel resistances with an increase in temperature

Figure 20: Graphs showing the temperature dependence of R_P, R_{AP} and TMR

Device four of this sample also had its TMR tested at different temperatures, the result of which is Figure [20a]. One striking feature of these results is the decrease in coercivity of only the hard ferromagnet, assumed to be cobalt as permalloy is particularly well known for being a soft ferromagnet

[38]. In cobalt it is a good generalization to say that coercivity is largely determined by magnetocrystalline and shape anisotropy contributions as they are much greater than the influence of other factors. Out of the two, magnetocrystalline anisotropy is strongly temperature dependent. In its hcp structure magnetocrystalline anisotropy energy is given as $E_a = K_{u1} sin^2\theta + K_{u2} sin^4\theta$ where K_{u1} and K_{u2} are constants and θ is the angle of magnetization relative to the c axis. K_{u2} is shown experimentally to decrease with an increase in temperature and, although not relevant to this set of data, K_{u1} even becomes negative after 520 K [39]. A lower magnetocrystalline anisotropy energy makes it easier for the magnetization orientation to switch resulting in a lower coercive field. In contrast the very reason why permalloy is a soft ferromagnet is its lack of magnetocrystalline anisotropy regardless of crystal structure [38]. As a result its coercivity, governed by other factors such as shape anisotropy and defects, is largely temperature independent.

The even more striking feature of Figure [20a] is the large drop in TMR as temperature is increased. The reasons for this have been built up over the last few paragraphs, all that is left to do is connect the dots. It was explained in Subchapter [5.1] that there are many conduction mechanisms aside from direct tunneling which provide an easier path for electrons to be transported to the opposite electrode. The relevant ones include trap assisted tunneling, pinhole transport, phonon and magnon assisted tunneling. Using a parallel resistor model in Subchapter [5.2] it was shown that the presence of these alternative conduction paths has a greater resistance lowering effect on the anti parallel configuration resistance leading to a lowering of TMR. Subchapter [5.1] also showed and explained theoretically that as temperature increased the influence of these conduction paths increased leading to a decrease in resistance. This can be seen as a lowering of the parallel resistances added to direct tunneling with temperature, leading to a decrease in TMR with T. Furthermore, Subchapter [5.2] explained the influence of magnon assisted tunneling at the low voltages used for the collection of these results (TMR vs T measurements were taken at 15 mV). It also explained that due to spin conservation the processes of magnon absorption and creation lead to the flipping of spins which decrease resistance in the anti parallel state and increase it in the parallel state. S. Zhang and P. M. Levy's model also shows a $T \cdot ln(T)$ temperature dependence of both P and AP conductivities multiplied by their respective spin flipping influenced densities of states -$(\rho^{min})^2 + (\rho^{maj})^2$ for AP and $2\rho^{min}\rho^{maj}$ for P assuming $\rho_L^{(min/maj)} = \rho_R^{(min/maj)}$ for simplicity- [36]. This leads to a greater increase in conductance for the AP state leading to a further decrease in TMR with T. Figure [20b] highlights the decrease of parallel and anti parallel resistance with temperature observed in the reduced dataset collected. The greater influence of temperature on the anti parallel state resistance is clearly observable, confirming what is expected in theory. However as only three data points were collected no reliable conclusions can be drawn by observing the trend itself. Another version of Figure [20b] which includes the previously discussed discarded data points is available in Appendix [A]. This figure does show a closer resemblance to trends observed in similar experiments done by other groups also pictured in Appendix [A], however as the measurements were faulty no conclusions will be drawn from it.

6 Conclusion

Throughout the course of this report the growth of eight samples of metal/insulator/metal and magnetic tunnel junctions was detailed. It was found that using electron beam evaporation tunneling characteristics are easily achievable, however the fabrication of magnetic tunnel junctions requires a full dedicated optimization of every parameter from the growth rate to the oxidation time. Nonetheless a TMR of up to 3.46 % was achieved and its inverse dependence on potential bias and temperature was investigated and confirmed. Although limited in scale, these studies matched theoretical explanations well, showcasing the ”zero bias anomaly” originating from magnon excitations as well as acting as a good source of identification of the presence of a large number of pinholes in the chosen design. This study serves as a jumping off point to honing the fabrication of amorphous MTJs, with the aim of future, more in depth research into the physical mechanisms that make magnetic tunnel junctions one of the most sought after technologies birthed by modern nanophysics.

6.1 Outlook

Fabrication Method Improvements: As the results obtained from the devices fabricated with this method were found to be consistent with the formation of multiple pinholes, either the current fabrication method must be optimized or another should be formulated. There were multiple factors that could have contributed to the poor growth of the tunnel barrier. Pinholes can result from non oxidized aluminum in the tunnel barrier, as such it is imperative to optimize the tunnel barrier oxidation time. As a 2 nm thickness was shown to work for the purpose of obtaining a TMR this can be kept constant and multiple samples can be fabricated implementing a range of oxidation times. As three total minutes still exhibited pinholes it seems reasonable to use it as a starting point and increase from there. Sample seven, meant for this very purpose, showed that five total minutes already fully saturated the oxidation the 2 nm of oxide as when the probes of the Keysight were placed on it, near insulator behavior was observed, thus five minutes should be the limit. The very same sample however also showed that when placing the contacts on the gold pads the resistance dropped dramatically. This was most likely due to the very low uniformity of gold growth on aluminum oxide creating defects where current can accumulate and form an electric field that aids conduction. As such the growth uniformity of both bottom and top electrodes is crucial for avoiding spin independent conduction. For this purpose, multiple samples can be fabricated keeping pressure and growth rate of the electrodes as low as possible and varying their height, as often times island growth smooths out with increasing layer thickness. It is also possible to experiment with different annealing temperatures and times for all layers, however it is important to keep in mind that higher temperatures can cause inter-diffusion between layers and chemical reactions not possible at room temperature. While AFM imaging can be used to monitor the roughness of the layers through roughness data, transmission electron microscopy (TEM) would be a much more powerful tool to shed light on the quality of the interface itself. All of these tests would take a great deal of time considering eight depositions were the absolute maximum achievable during the ten working weeks of fabrication time. As such it would be useful to first optimize the junction design itself. For example, a lower junction area would decrease the number of pinholes and a thin layer of Ta below Co has been used in successful MTJ experiments to induce more layer like growth. Alternative fabrication methods known for slower, more layer like growth can also be employed such as molecular beam epitaxy, however this would not only greatly increase fabrication times, but also comes with a new, yet unexplored set of challenges. Lastly, on a more technical note, the shape of the plasma ring employed caused uneven plasma formation and oxidation of the devices, an easy improvement would be to replace it with a fully circular ring to be mounted in the

center of the product chamber. Furthermore, to ensure accurate deposition rates, sample fabrications must be done ensuring an adequate filling of the evaporated materials.

Interesting Followup Research: MOKE or SQUID setups could be used to obtain hysteresis loops for the devices to compare with the TMR graphs obtained using Bloch. Using lock in amplifiers and sending a small AC signal superimposed on the standard DC signal used for the I-V sweeps throughout this report it is possible to directly measure the first derivative of the I-Vs -thus conductance G(V)- as proportional to the first harmonic of the resulting signal [10]. By combining these two methods it is possible to perform a G(V) sweep in the parallel and anti parallel states and obtain a much fuller data set of TMR bias dependency. With the help of a script that runs this sweep at many temperatures between 77 K and 300 K a full TMR vs T dataset can be obtained. Consequently it would also be possible to calculate the maximum energy of magnons in both electrodes and see if it matches with the end of the linear regime of the potential bias dependency data. Furthermore alpha and gamma for the temperature dependency fit described by Chang He Shang et.al. can be obtained and gamma minimized as a faster way to gauge the quality of the barrier than TEM. This would however require to know the exact spin polarizations of both electrodes. It is possible to obtain such information if a high quality MTJ is produced with electrodes of the same material, in that case P can be obtained from Julliere's equation at low temperature and bias. Through such devices it would also be possible to insert a non ferromagnetic or antiferromagnetic layer of varying thickness in between one electrode and the tunnel barrier to observe its effect on the TMR. There are a myriad of other experiments to run on these devices, however, for the sake of applications their low TMR has been surpassed by devices with novel electrode and barrier materials. In this context it would be appropriate to begin attempts at the fabrication of more modern crystalline MgO MTJs which exhibit much greater TMR values thanks to their symmetry filtering capabilities [4].

Bibliography

[1] M. Julliere, "Tunneling between ferromagnetic films," *Physics Letters A*, vol. 54, pp. 225–226, 1975.

[2] J. S. Moodera, L. R. Kinder, T. M. Wong, and R. Meservey, "Large magnetoresistance at room temperature in ferromagnetic thin film tunnel junctions," *Phys. Rev. Lett.*, vol. 74, pp. 3273–3276, Apr 1995.

[3] T. Miyazaki and N. Tezuka, "Giant magnetic tunneling effect in fe/al2o3/fe junction," *Journal of Magnetism and Magnetic Materials*, vol. 139, no. 3, pp. L231–L234, 1995.

[4] S. S. P. Parkin, C. Kaiser, A. Panchula, P. M. Rice, B. Hughes, M. Samant, and S.-H. Yang, "Giant tunnelling magnetoresistance at room temperature with mgo (100) tunnel barriers," *Nature Materials*, vol. 3, p. 862–867, 2004.

[5] S. Bhatti, R. Sbiaa, A. Hirohata, H. Ohno, S. Fukami, and S. Piramanayagam, "Spintronics based random access memory: a review," *Materials Today*, vol. 20, no. 9, pp. 530–548, 2017.

[6] P. Atkins and R. Friedman, *Molecular Quantum Mechanics*. New York: OXFORD University Press, 5 ed., 2011.

[7] R. Meservey and P. Tedrow, "Spin-polarized electron tunneling," *Physics Reports*, vol. 238, no. 4, pp. 173–243, 1994.

[8] J. G. Simmons, "Generalized formula for the electric tunnel effect between similar electrodes separated by a thin insulating film," *Journal of Applied Physics*, vol. 34, pp. 1793–1803, 06 1963.

[9] A. Akhmerov, "Wkb approximation," 11 2019. Available online: `https://appquantmech.quantumtinkerer.tudelft.nl/wkb$_$tunnel/`.

[10] P. LeClair, *Fundamental aspects of spin polarized tunneling : magnetic tunnel junctions and spin filters*. Phd thesis 1 (research tu/e / graduation tu/e), Applied Physics and Science Education, 2002.

[11] W. F. Brinkman, R. C. Dynes, and J. M. Rowell, "Tunneling conductance of asymmetrical barriers," *Journal of Applied Physics*, vol. 41, pp. 1915–1921, 04 1970.

[12] I. Giaever, "Energy gap in superconductors measured by electron tunneling," *Phys. Rev. Lett.*, vol. 5, pp. 147–148, Aug 1960.

[13] W. A. Harrison, "Tunneling from an independent-particle point of view," *Phys. Rev.*, vol. 123, pp. 85–89, Jul 1961.

[14] J. Bardeen, "Tunnelling from a many-particle point of view," *Phys. Rev. Lett.*, vol. 6, pp. 57–59, Jan 1961.

[15] D. J. Griffiths, *Introduction to Electrodynamics*. Cambridge: CAMBRIDGE University Press, 4 ed., 2017.

[16] C. Kittel, *Introduction to Solid State Physics*. Hoboken, NJ: Jhon Wiley Sons, Inc., 8 ed., 2005.

[17] B. M. Moskowitz, "Hitchhiker's guide to magnetism," 06 1991. Available online: https://cse.umn.edu/irm/3-magnetic-anisotropy.

[18] B. Doudin and J.-P. Ansermet, "Nanostructuring materials for spin electronics," *Europhysics news*, vol. 28, 09 1997.

[19] E. C. S. F. R. S, "Ferromagnetism," *Reports on Progress in Physics*, vol. 11, 01 1947.

[20] D. Mazumdar, "Stoner model of ferromagnetism for electron gas," 2019. Available online: https://www2.physics.siu.edu/~dmazumdar/575_magnetism.html.

[21] A. Vitale, J. Wörnle, and A. L. V. dos Reis, "Case study- device physics." Submitted as coursework for [Device Physics], Rijksuniversiteit Groningen, April 2025, 2025.

[22] N. Maiti, P. Karmakar, U. Barve, and A. Bapat, "An evaporation system for film deposition using electron beam sources," *Journal of Physics: Conference Series*, vol. 114, 05 2008.

[23] F. Temescal, "Temescal fc2000 / bjd-2000 bell jar deposition system," 2025. Available online: https://temescal.ferrotec.com/systems/fcbjd-2000/.

[24] A. W. Campbell, "Ionization," 02 2011. Available online: https://www.thermopedia.com/content/885/.

[25] S. Gourrier and M. Bacal, "Review of oxide formation in a plasma," *Plasma Chemistry and Plasma Processing*, vol. 1, pp. 217–232, 09 1981.

[26] Tektronix, "Two-wire vs. four-wire resistance measurements: Which configuration makes sense?," 2023. https://www.tek.com/en/documents/technical-article/two-wire-vs-four-wire-resistance-measurements-which-configuration-makes-s.

[27] G. Burger, E. Smulders, J. Berenschot, T. Lammerink, J. Fluitman, and S. Imai, "High-resolution shadow-mask patterning in deep holes and its application to an electrical wafer feed-through," *Sensors and Actuators A: Physical*, vol. 54, no. 1, pp. 669–673, 1996.

[28] P. La Torraca, A. Padovani, L.-E. Wernersson, K. Cherkaoui, P. Hurley, and L. Larcher, "Electrically active defects in al2o3-ingaas mos stacks at cryogenic temperatures," in *2023 IEEE International Integrated Reliability Workshop (IIRW)*, pp. 1–5, 2023.

[29] F.-C. Chiu, "A review on conduction mechanisms in dielectric films," *Advances in Materials Science and Engineering*, vol. 2014, no. 1, p. 578168, 2014.

[30] P. Guo, D. L. Li, J. F. Feng, H. Kurt, G. Q. Yu, J. Y. Chen, H. X. Wei, J. M. D. Coey, and X. F. Han, "Conductance enhancement due to interface magnons in electron-beam evaporated mgo magnetic tunnel junctions with cofeb free layer deposited at different pressure," *Journal of Applied Physics*, vol. 116, p. 153905, 10 2014.

[31] O. V. Snigirev, A. M. Tishin, K. E. Andreev, S. A. Gudoshnikov, and J. Bohr, "Magnetic properties of ultrathin ni films," *Physics of the Solid State*, vol. 40, pp. 1550–1553, 1998.

[32] E. Verduijn, *Spin polarization measurements using ferromagnet-insulator-superconductor junctions*. Masters thesis, Applied Physics and Science Education, 2002.

[33] L. Bocklage, J. M. Scholtyssek, U. Merkt, and G. Meier, "Spin polarization of ni2mnin and ni80fe20 determined by point-contact andreev spectroscopy," *Journal of Applied Physics*, vol. 101, p. 09J512, 05 2007.

[34] X. Chen and R. H. Victora, "Effect of pinholes in magnetic tunnel junctions," *Applied Physics Letters*, vol. 91, 11 2007.

[35] S. O. Valenzuela, D. J. Monsma, C. M. Marcus, V. Narayanamurti, and M. Tinkham, "Spin polarized tunneling at finite bias," *Phys. Rev. Lett.*, vol. 94, May 2005.

[36] S. Zhang, P. M. Levy, A. C. Marley, and S. S. P. Parkin, "Quenching of magnetoresistance by hot electrons in magnetic tunnel junctions," *Phys. Rev. Lett.*, vol. 79, pp. 3744–3747, Nov 1997.

[37] E. McCann and V. I. Fal'ko, "Magnon-assisted transport and thermopower in ferromagnet–normal-metal tunnel junctions," *Phys. Rev. B*, vol. 68, p. 172404, Nov 2003.

[38] L. F. Yin, D. H. Wei, N. Lei, L. H. Zhou, C. S. Tian, G. S. Dong, X. F. Jin, L. P. Guo, Q. J. Jia, and R. Q. Wu, "Magnetocrystalline anisotropy in permalloy revisited," *Phys. Rev. Lett.*, vol. 97, p. 067203, Aug 2006.

[39] K. Ait Atmane, F. Zighem, Y. Soumare, M. Ibrahim, R. Boubekri, T. Maurer, J. Margueritat, J.-Y. Piquemal, F. Ott, G. Chaboussant, F. Schoenstein, N. Jouini, and G. Viau, "High temperature structural and magnetic properties of cobalt nanorods," *Journal of Solid State Chemistry*, vol. 197, p. 297–303, Jan. 2013.

[40] A. Yahyaoui, A. Elsharabasy, J. Yousaf, K. Sedraoui, and H. Rmili, "Miim-based optical log spiral rectenna for efficient ir energy harvesting," *Alexandria Engineering Journal*, vol. 61, 02 2022.

[41] R. Rajput and R. Vaid, "Flash memory devices with metal floating gate/metal nanocrystals as the charge storage layer: A status review," *Facta universitatis - series: Electronics and Energetics*, vol. 33, pp. 155–167, 01 2020.

Appendices

A Discarded Temperature Dependency Graphs

The following graphs displaying the magnetic field sweeps of sample eight at 125 K, 150 K, 200 K, 250 k and 300 K were discarded due to the mismatch between the resistance values of one peak compared to the other. This mismatch was due to not having allowed the sample to stabilize at the chosen temperature. This resulted in a magnetic field sweep where temperature kept rising, thus the resistance decreased, as the data was being collected.

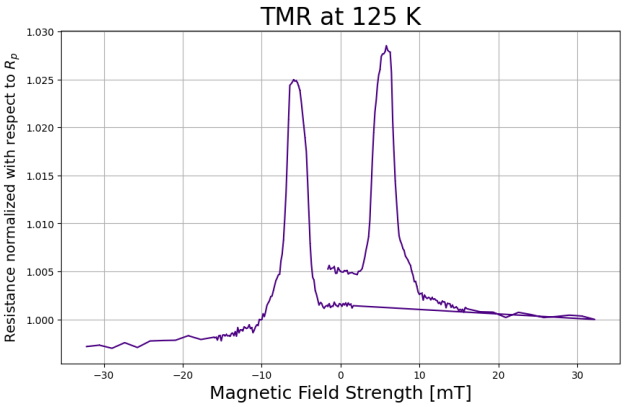

(a) Magnetic field sweep performed at 125 K

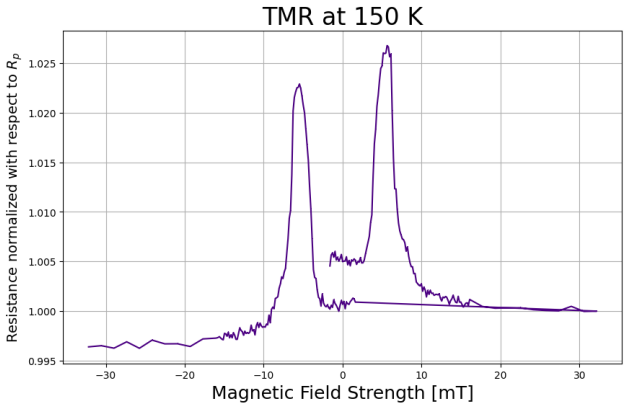

(b) Magnetic field sweep performed at 150 K

Figure 21: Discarded magnetic field sweeps for temperature dependency measurements, here pictured 125 K and 150 K

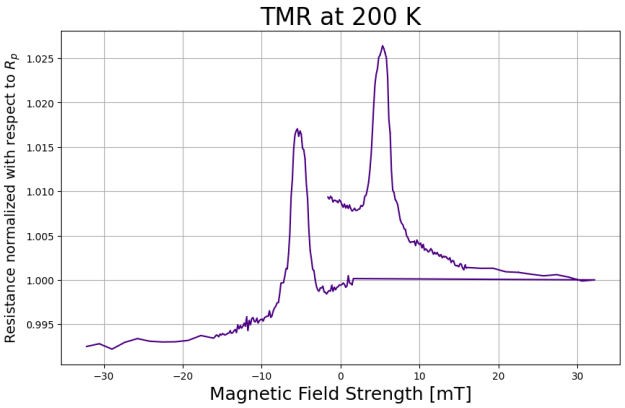

(a) Magnetic field sweep performed at 200 K

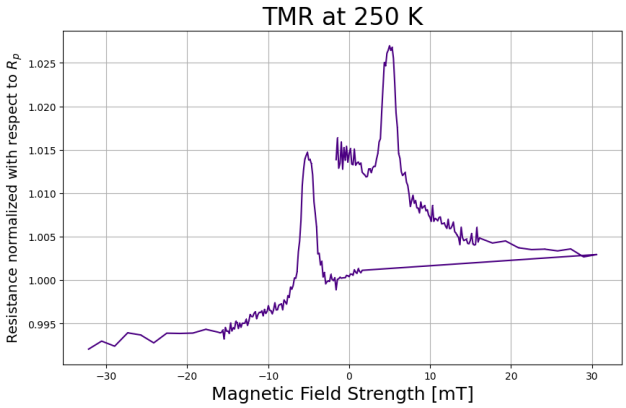

(b) Magnetic field sweep performed at 250 K

Figure 22: Discarded magnetic field sweeps for temperature dependency measurements, here pictured 200 K and 250 K

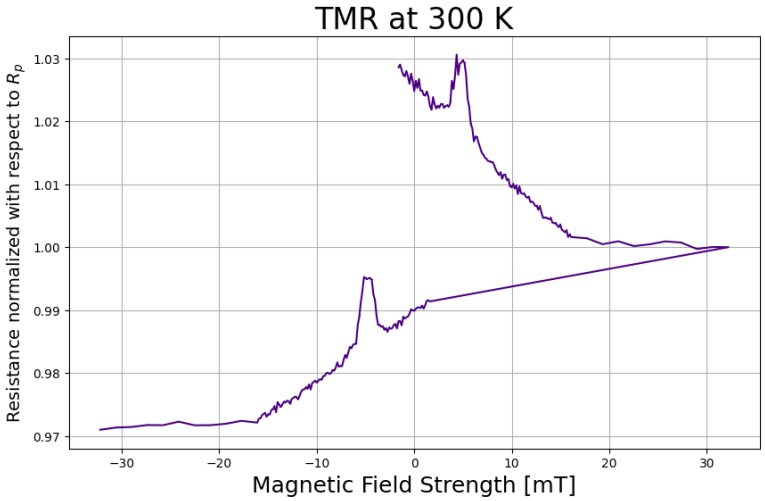

Figure 23: Discarded magnetic field sweep performed at 300 K

Below is also pictured the temperature dependence of parallel and anti parallel resistances including points for the discarded data above:

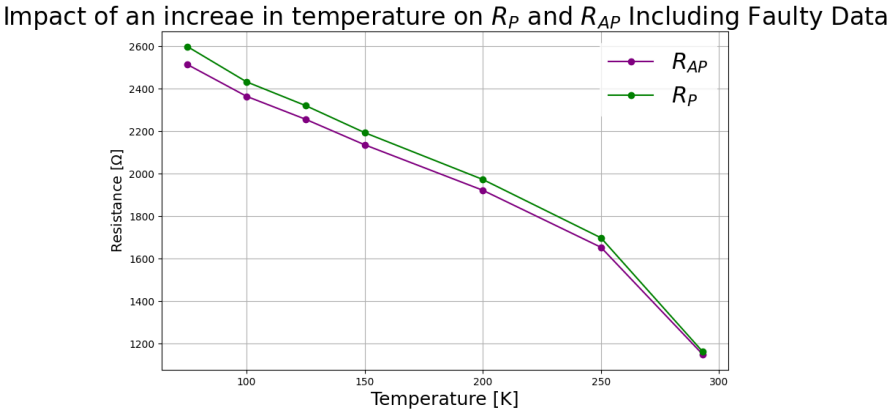

Figure 24: Graph displaying the temperature dependence of R_{AP} and R_P including data points for discarded magnetic field sweeps

This follows the temperature dependence of these resistances obtained by other research groups more closely as can be seen below:

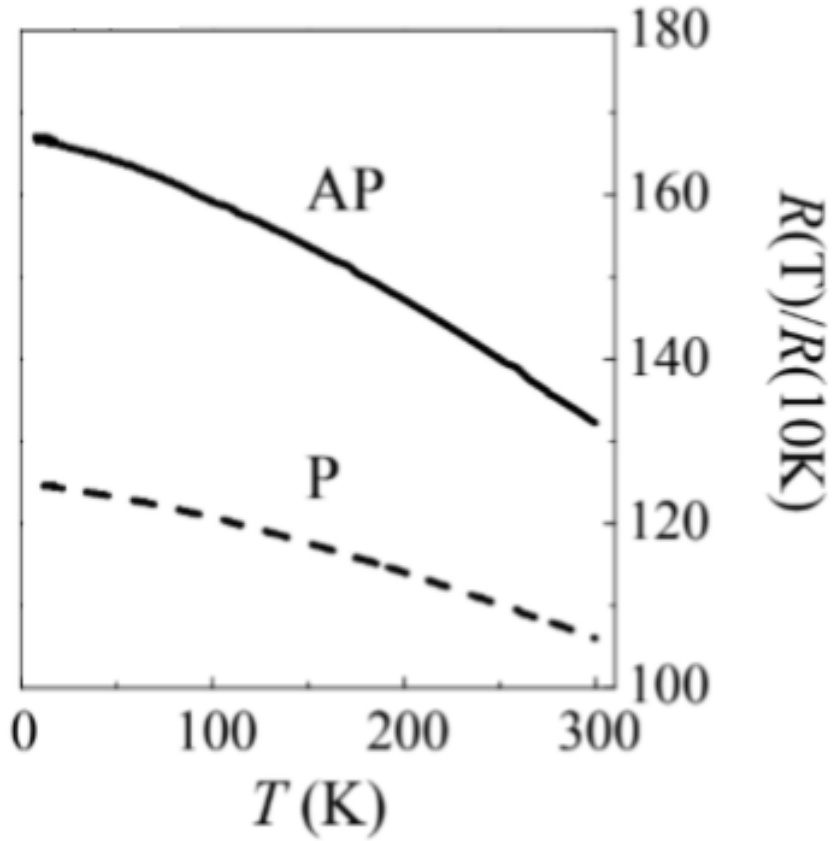

Figure 25: Graph displaying the temperature dependence of R_{AP} and R_P presented LeClair in his thesis and obtained in an unpublished work attributed to him and other colleagues [10]

B Code Utilized

To fit the temperature dependent I-Vs of the M/I/M junction to the Simmons model I used the following code (here presented for 293 K). The necessary packages were imported, the data was opened from google drive and appended to a list, subsequently made into an array, fit using the Simmons formula and graphed along with the fit curve.

```
x293 = []
y293 = []

for line in open('/content/drive/MyDrive/Bachelor Project/Data Analysis/Data/MIM/Temperature Dependent IV/2_probe_IV_D3_Vsrc(pn100mV)_p14n12_101pts_293K_012_data.dat', 'r'):
lines = [i for i in line.strip().split('\t')]
x293.append(float(lines[0]))
y293.append(float(lines[1]))

X293d=np.array(x293)
Y293d=np.array(y293)
```

A = 8.5278*10**(-7)
def simmons$_m odeld(V, phi)$:
$dd = 4 * 10 * *(-9)$
$return((A * c.e)/(2 * c.pi * c.h * (dd * *2))) * ((phi - c.e * V/2) * np.exp(-(4 * c.pi * dd/c.h) * np.sqrt(2 * c.electron_mass) * np.sqrt(phi - c.e * V/2)) - (phi + c.e * V/2) * np.exp(-(4 * c.pi * dd/c.h) * np.sqrt(2 * c.electron_mass) * np.sqrt(phi + c.e * V/2)))$

initial$_p hi_g uess293 = 0.55 * c.e$

popt293d, pcov293d = curve$_f it(simmons_m odeld, X293d, Y293d, p0 = [initial_p hi_g uess293])$

phi$_f it293d = popt293d[0]$
$print(f"Best fitted barrier height : phi_f it293d/c.e : .3feV")$

plt.title("Fitting of IV characteristics of device 3 to simmons model (only phi, d = 4 nm) at 293 K")
plt.xlabel('Voltage [V]')
plt.ylabel('Current [A]')

x$_t icks = np.arange(-0.150, 0.150 + 0.05, 0.05)$
$plt.xticks(x_t icks)$
$plt.grid()$
$plt.plot(x293, y293, marker = ',', c = ' b', label = ' Data')$
$plt.plot(x293, simmons_m odeld(X293d, phi_f it293d), marker = ',', c = ' r', label = f'simmons fit : phi_f it293d/c.e : .3feV')$
$leg = plt.legend()$
$leg.get_f rame().set_a lpha(0)$
$plt.show()$

To plot the TMR vs potential bias graph the following code was used. Each curve is normalized with its parallel resistance.
x15 = []
y15 = []
x25 = []
y25 = []
x35 = []
y35 = []
x45 = []
y45 = []
x55 = []
y55 = []

for line in open('/content/drive/MyDrive/Bachelor Project/Data Analysis/Data/MTJ/MTJ Bias Dependence/IVs_withB_D2_Vsrc16p13n(pn15mV)_Isens(p15n19)_75K_029_data.dat', 'r'):
lines = [i for i in line.strip().split('\t')]
x15.append(float(lines[0]))
y15.append(float(lines[1]))

```
for line in open('/content/drive/MyDrive/Bachelor Project/Data Analysis/Data/MTJ/MTJ Bias Dependence/IVs_withB_D2_Vsrc16p13n(pn25mV)_Isens(p15n19)_75K_025_data.dat', 'r'):
lines = [i for i in line.strip().split('\t')]
x25.append(float(lines[0]))
y25.append(float(lines[1]))
for line in open('/content/drive/MyDrive/Bachelor Project/Data Analysis/Data/MTJ/MTJ Bias Dependence/IVs_withB_D2_Vsrc16p13n(pn35mV)_Isens(p15n19)_75K_026_data.dat', 'r'):
lines = [i for i in line.strip().split('\t')]
x35.append(float(lines[0]))
y35.append(float(lines[1]))
for line in open('/content/drive/MyDrive/Bachelor Project/Data Analysis/Data/MTJ/MTJ Bias Dependence/IVs_withB_D2_Vsrc16p13n(pn45mV)_Isens(p15n19)_75K_027_data.dat', 'r'):
lines = [i for i in line.strip().split('\t')]
x45.append(float(lines[0]))
y45.append(float(lines[1]))
for line in open('/content/drive/MyDrive/Bachelor Project/Data Analysis/Data/MTJ/MTJ Bias Dependence/IVs_withB_D2_Vsrc16p13n(pn55mV)_Isens(p15n19)_75K_028_data.dat', 'r'):
lines = [i for i in line.strip().split('\t')]
x55.append(float(lines[0]))
y55.append(float(lines[1]))

plt.figure(figsize=(10, 6))

plt.title("Bias Voltage Dependence of TMR at 75 K", fontsize = 24)
plt.xlabel('Magnetic Field Strength [mT]', fontsize = 18)
plt.ylabel(r'Resistance normalized with respect to $R_p$', fontsize = 14)

plt.grid()
plt.plot(np.array(x15) * 16.09375, (0.015/np.array(y15))/(0.015/1.015239E-5), marker = ',', c = '800080',
label='15 mV - 2.48 % TMR')
plt.plot(np.array(x25) * 16.09375, (0.025/np.array(y25))/(0.025/1.719308E-5), marker = ',', c = '00008B',
label='25 mV - 2.37 % TMR')
plt.plot(np.array(x35) * 16.09375, (0.035/np.array(y35))/(0.035/2.467775E-5), marker = ',', c = '008000',
label='35 mV - 2.29 % TMR')
plt.plot(np.array(x45) * 16.09375, (0.045/np.array(y45))/(0.045/3.264391E-5), marker = ',', c = 'FFD700',
label='45 mV - 2.15 % TMR')
plt.plot(np.array(x55) * 16.09375, (0.055/np.array(y55))/(0.055/4.119341E-5), marker = ',', c = 'E50000',
label='55 mV - 2.06 % TMR')
leg = plt.legend()
leg.get_frame().set_edgecolor('none')
leg.get_frame().set_facecolor('white')
plt.show()
```

The same code was also used to create the TMR vs temperature graph.

An ideal expected resistance was calculated for Sample eight, the following is the code that was used to obtain it:

def simmons$_m$odelA(V,A,phi,d) :
$return((A*c.e)/(2*c.pi*c.h*(d**2)))*((phi-c.e*V/2)*np.exp(-(4*c.pi*d/c.h)*np.sqrt(2*c.electron_mass)*np.sqrt(phi-c.e*V/2))-(phi+c.e*V/2)*np.exp(-(4*c.pi*d/c.h)*np.sqrt(2*c.electron_mass)*np.sqrt(phi+c.e*V/2)))$

print (simmons$_m$odelA$(2*10**(-4),8.5278*10**(-7),2*c.e,2*10**(-9)))$

C Ideal Barrier Height Calculation

This was done simply by subtracting aluminum oxide's electron affinity (2.58 eV [40]) from cobalt and $Ni_{80}Fe_{20}$'s work functions (5 eV for Co and between 5 eV and 4.7 eV for $Ni_{80}Fe_{20}$ [41]) resulting in $\overline{\phi}$ = 2.4 eV. As This is not an exact estimation, and rel tunnel barrier heights tend to be smaller due to defects even for very clean barriers, the barrier height was rounded down to 2 eV.